A MESHFREE UNIT-CELL METHOD FOR EFFECTIVE PLANAR ANALYSIS OF CELLULAR BEAMS

A.R. Zainal Abidin[a,b], **B.A. Izzuddin**[a,*], **F. Lancaster**[a,c]

[a] Department of Civil and Environmental Engineering, Imperial College, London SW7 2AZ, United Kingdom

[b] Faculty of Civil Engineering, Universiti Teknologi Malaysia, 81310 Skudai, Johor, Malaysia

[c] Eckersley O'Callaghan, 137 Varick Street, #406, New York, NY 10013

[*] Corresponding author: b.izzuddin@imperial.ac.uk

Abstract

This paper presents a novel approach for accurate and efficient planar response analysis of cellular beams, which provides the necessary input for local out-of-plane buckling analysis of web components. The proposed approach utilises the super-element concept defined for unit-cells, achieving further efficiencies through an enhanced Element-Free Galerkin (EFG) approach for establishing the planar super-element response. Several examples are presented, firstly at the level of unit-cells, where the computational benefits of the EFG method are highlighted, and finally at the overall level of cellular beams, where the superior performance of the unit-cell approach with virtually no compromise in accuracy is demonstrated.

Keywords: Meshfree methods; Element-free Galerkin method; Planar Response; Cellular beams; Unit-cell formulation

1. Introduction

Cellular beams have become in recent years a popular form of steel construction, largely due to enabling large spans while facilitating the integration of services within the floor depth [1-3]. As illustrated in Figure 1, cellular beams are easily fabricated from standard I-beams through appropriate cutting, offsetting and joining operations, enhancing the bending stiffness and resistance via an increased distance between the flanges, while reducing weight via the resulting openings in the web.

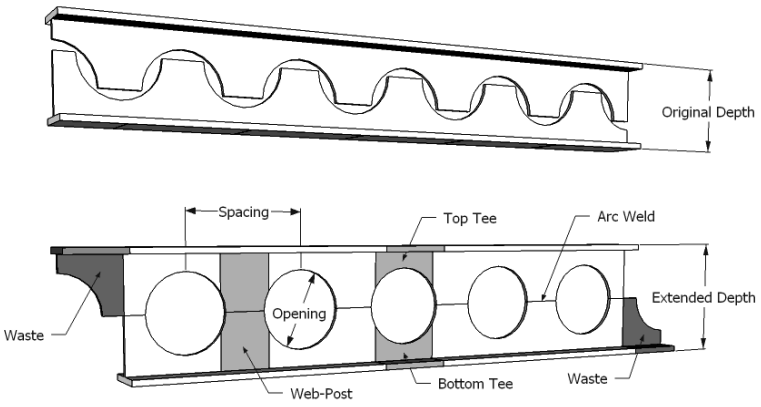

Figure 1 – Typical profiling of cellular beams

Besides the above relative structural benefits of cellular beams, their structural response is very different in certain respects from the parent I-beam [4]. The existence of regular holes influences the structural behaviour particularly in the web region where local elements, such as the web-posts and top/bottom tees, are subject to local actions throughout the beam span. These actions consist of not only contributions to the overall cross-sectional shear and bending moment, but are also superimposed by secondary effects leading to a highly nonlinear stress distribution over the cellular beam depth and length [5, 6]. One of the most important and distinctive structural characteristics of cellular beams relates to local buckling of the web elements [6-9], which in turn depends on the nonlinear distribution of planar stresses in the perforated web.

Although some guidance on the design and assessment of cellular beams is provided in codes of practice [10, 11], the selection and design of cellular beams is typically undertaken in practice with the aid of specialist software (e.g. [12]). However, in considering the local buckling of web elements, simplified models were adopted [13-17] , utilising for example a strut buckling analogy with empirical calibration against nonlinear finite element models [18-20]. While the resulting simplified models are computationally efficient, these are not rational and sufficiently general for application to a wide range

of cellular beam geometric configurations, as they ignore both the nonlinear planar stress distribution and the two-dimensional plate buckling behaviour of the web components. Of course, accurate predictions can be achieved in this respect using nonlinear finite element analysis, though the computational and modelling demands of such an approach are still prohibitive for application in design practice.

The present work is motivated by the need for an efficient and practical modelling approach for predicting the nonlinear planar stress distribution in cellular beams, which could in turn be used for local buckling assessment of the web components in a separate model of the nonlinear out-of-plane response. Focusing on elastic local buckling as a performance consideration that may be used along with material strength limit for cellular beam design, this paper is mainly concerned with the accurate and efficient determination of the nonlinear planar stress distribution in cellular beams arising under planar loads within the linear elastic range. The assessment of local buckling could then be undertaken considering the out-of-plane geometric stiffness associated with the predicted planar stress distribution as well as the out-of-plane material stiffness, though this aspect is not covered in the present paper but is referred to previous work by the authors on beams with irregular openings [21].

For an accurate prediction of the nonlinear planar stress distribution in linear elastic cellular beams, the most obvious approach is to utilise finite element analysis, though this can still be computationally demanding for typical cellular beams, even in the linear elastic range. Meshfree methods have recently emerged as an alternative approach [22-24] with potentially significant relative benefits, particularly where geometric features complicate the meshing with finite elements, as in the case of beams with openings. Moreover, in such cases, the meshfree approach has the potential to achieve significant computational savings with a considerable reduction in the number of degrees of freedom (DOF) for comparable accuracy to finite element analysis.

Amongst the various meshfree methods, the element-free Galerkin (EFG) method [25] and the meshless local Petrov-Galerkin (MLPG) method [26] have been considered for the present work. In contrast with the MLPG method which is claimed as ‘truly meshless’, the EFG method requires ‘background cells’ for numerical integration of the governing equation over the problem domain. While this may be seen as a shortcoming for the EFG method, it is actually a benefit in the present context, since the evaluation of planar stresses at a fixed set of integration points, rather than a variable set associated with the testing function as in the MLPG method, is required for determining the out-of-plane geometric stiffness in subsequent local buckling assessment. Furthermore, the MLPG method suffers from the fact that rigid body testing modes are not accurately represented, leading to only an approximate satisfaction of equilibrium between the applied loading and the reactions at the support boundaries. Accordingly, the EFG method is selected with due consideration of its following benefits:

(i) it is a meshless method that can be easily applied to complex geometric domains, (ii) it facilitates numerical integration via the use of fixed integration points over the domain, and (iii) it ensures external equilibrium at sub-domain level between loading and boundary actions.

Besides the selection of the EFG approach, this work capitalises on a major characteristic of cellular beams, which is the repetitive nature of the holes over the beam length, thus introducing the notion of a unit-cell as a 'super-element' which interacts with adjacent unit-cells via a reduced number of DOF, as illustrated in Figure 2. Towards this end, the EFG method is adopted and suitably enhanced for planar analysis at the unit-cell level, while the overall response of the cellular beam is efficiently obtained via the assembly of super-element contributions.

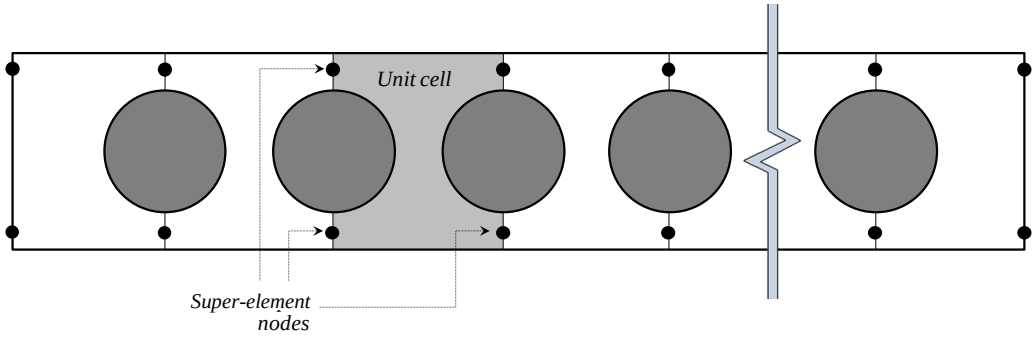

Figure 2 – Unit-based discretisation of cellular beam

The paper proceeds with presenting the numerical discretisation of a unit-cell using the EFG method, highlighting the enhancements undertaken for application to cellular beams. The formulation of the super-element associated with the unit-cell is then provided, including the treatment of edge unit-cells and the assembly of the overall cellular beam response. Finally, several examples are presented, ranging from the level of an individual unit-cell to a whole cellular beam, which demonstrate the accuracy and computational benefits of the proposed approach towards predicting the planar response of cellular beams.

2. Numerical Discretisation with EFG Method

The element-free Galerkin (EFG) method is used to discretise the problem domain at the unit cell level. The main feature of the EFG method is the utilisation of a smooth and continuous domain function via the application of a moving least squares (MLS) approach. As this MLS approximation requires only a set of nodes to generate shape functions, it is acknowledged as an element-free method which offers significant savings on computational effort, since a major cost of element meshing is

eliminated [25]. However, such benefit comes with some additional costs, especially in relation to the imposition of boundary conditions, since the MLS function does not represent the actual nodal values.

The EFG method is constructed on the basis of a Galerkin formulation with the adoption of moving least-squares approximation to produce the shape functions, as presented in detail by [25]. To view the application of EFG method in 2D solid mechanic problems, a domain of Ω with a boundary Γ, being in a state of equilibrium, is considered:

$$\boldsymbol{L}_d{}^{\mathrm{T}}\boldsymbol{\sigma} + \boldsymbol{b} = 0 \quad \text{in } \Omega \tag{1}$$

with boundary conditions specified as:

$$\begin{aligned} &\boldsymbol{u} = \bar{\boldsymbol{u}} \quad \text{on } \Gamma_{\mathrm{u}} \\ &\boldsymbol{L}_n\boldsymbol{\sigma} = \bar{\boldsymbol{t}} \quad \text{on } \Gamma_{\mathrm{t}} \end{aligned} \tag{2}$$

in which $\boldsymbol{\sigma}$ is the stress vector corresponding to the displacement fields, $\boldsymbol{L}_d$ is a matrix of differential operators for equilibrium, $\boldsymbol{L}_n$ is a matrix of the unit normal to the boundary Γ, and $\boldsymbol{b}$ is the body force of the domain Ω. $\bar{\boldsymbol{u}}$ and $\bar{\boldsymbol{t}}$ are the prescribed boundary displacements and tractions respectively. The well-known Galerkin weak form of the equilibrium Equation (1) is given as:

$$\int_{\Omega} \boldsymbol{\delta\varepsilon}^{\mathrm{T}} \cdot \boldsymbol{\sigma} \, \mathrm{d}\Omega - \int_{\Omega} \boldsymbol{\delta u}^{\mathrm{T}} \cdot \boldsymbol{b} \, \mathrm{d}\Omega - \int_{\Gamma_{\mathrm{t}}} \boldsymbol{\delta u}^{\mathrm{T}} \cdot \boldsymbol{t}_{\Gamma} \, \mathrm{d}\Gamma = 0 \qquad (\forall \boldsymbol{\delta u}) \tag{3}$$

or in the form of the displacements function $\boldsymbol{u}$:

$$\int_{\Omega} \left(\nabla_s \boldsymbol{\delta u}\right)^{\mathrm{T}} \cdot \mathbf{D} \cdot \left(\nabla_s \boldsymbol{u}\right) \, \mathrm{d}\Omega - \int_{\Omega} \boldsymbol{\delta u}^{\mathrm{T}} \cdot \boldsymbol{b} \, \mathrm{d}\Omega - \int_{\Gamma_{\mathrm{t}}} \boldsymbol{\delta u}^{\mathrm{T}} \cdot \boldsymbol{t}_{\Gamma} \, \mathrm{d}\Gamma = 0 \qquad (\forall \boldsymbol{\delta u}) \tag{4}$$

in which $\boldsymbol{u}$ is often defined in terms of shape functions ($\boldsymbol{N}^{\phi}$) and the nodal DOFs ($\mathbf{u}$):

$$\boldsymbol{u} = \boldsymbol{N}^{\phi}\mathbf{u} \tag{5}$$

Note that discretisation with the finite element method (FEM) uses an element-based approach to construct the pre-defined shape functions, for which a well-generated mesh is necessary to obtain a good approximation. This is always a major issue in the FEM particularly when dealing with irregular domains. The EFG method, on the other hand, benefits from the MLS numerical discretisation, in which only a free form of distributed local nodes is required and completely exempted from any element connectivity.

2.1. Shape functions by MLS approximation

The MLS approximation is a general technique of fitting a curve or surface to scattered data, which is commonly used in statistical analysis. In the EFG method, such a technique is enhanced to generate a higher-order surface fit function of displacements $u^h(\mathbf{x}_I)$ based on nodal values (u_I). This is accomplished by the use of a polynomial-based expansion defined as:

$$u^h(\mathbf{x}) = \sum_{j=1}^{m} p_j(\mathbf{x}) a_j(\mathbf{x}) \equiv \boldsymbol{p}^T(\mathbf{x})\boldsymbol{a}(\mathbf{x}) \tag{6}$$

in which $p_j(\mathbf{x})$ is the polynomial basis function with m number of terms, and $a_j(\mathbf{x})$ features as the unknown coefficients which perform curve-fitting. Both terms are a function of the space coordinates $\mathbf{x} = \begin{bmatrix} x & y \end{bmatrix}$. Considering Pascal's triangle of monomials, $p_j(\mathbf{x})$ simply reaches the desired degree of continuity by the employment of sufficient monomial terms. In this work, the quadratic basis is employed, hence $m = 6$, as given by:

$$\boldsymbol{p}^T(\mathbf{x}) = \begin{bmatrix} 1, x, y, x^2, xy, y^2 \end{bmatrix} \tag{7}$$

On the other hand, $a_j(\mathbf{x})$ is an arbitrary set of coefficients that needs to be solved, and yet it should not be taken as a constant for accuracy reason [25]. Therefore, in solving for the unknown coefficients, a functional of weighted residuals between the actual nodal parameters (u_I) and their approximated values, $u^h(\mathbf{x}_I)$, is used:

$$\Delta = \sum_{I=1}^{N} w(\mathbf{x} - \mathbf{x}_I)\left[u^h(\mathbf{x}_I) - u_I \right]^2 \tag{8}$$

where N is the number of local nodes, $w(\mathbf{x} - \mathbf{x}_I)$ is a built-in weight function that determines the influence of the residuals at different nodes ($\mathbf{x}_I$) around the focus point ($\mathbf{x}$).

Considering Equations (6) and (8), the selection of $\boldsymbol{a}(\mathbf{x})$ that minimises the residual functional can be obtained from the condition of stationary Δ with respect to $\boldsymbol{a}(\mathbf{x})$, which leads to the following solution of a linear equation:

$$\boldsymbol{A}(\mathbf{x})\boldsymbol{a}(\mathbf{x}) = \boldsymbol{B}(\mathbf{x})\mathbf{u} \Rightarrow \boldsymbol{a}(\mathbf{x}) = \left(\boldsymbol{A}(\mathbf{x})^{-1} \boldsymbol{B}(\mathbf{x}) \right)\mathbf{u} \tag{9}$$

where:

$$\boldsymbol{A}(\mathbf{x}) = \sum_{I=1}^{\mathrm{N}} w(\mathbf{x}-\mathbf{x}_I)\,\boldsymbol{p}(\mathbf{x}_I)\,\boldsymbol{p}^{\mathrm{T}}(\mathbf{x}_I)$$
$$\boldsymbol{B}(\mathbf{x}) = \left[\boldsymbol{b}_1, \quad \cdots, \quad \boldsymbol{b}_{\mathrm{N}}\right], \; \boldsymbol{b}_I = w(\mathbf{x}-\mathbf{x}_I)\,\boldsymbol{p}(\mathbf{x}_I) \tag{10}$$

Finally, by considering Equation (9), the initial Equation (6) can be rewritten in terms of the nodal parameters (**u**) and their corresponding shape functions (ϕ_I) as follows:

$$u^h(\mathbf{x}) = \sum_{j=1}^{\mathrm{m}} p_j(\mathbf{x})a_j(\mathbf{x}) \; = \sum_{I=1}^{\mathrm{N}}\sum_{j=1}^{\mathrm{m}} p_j(\mathbf{x})\left(\boldsymbol{A}^{-1}(\mathbf{x})\boldsymbol{B}(\mathbf{x})\right)_{jI}\mathrm{u}_I \; = \sum_{I=1}^{\mathrm{N}}\phi_I(\mathbf{x})\;\mathrm{u}_I \; = \boldsymbol{\Phi}\mathbf{u} \tag{11}$$

where **u** is a vector of nodal displacements (I = 1, 2, ... , N) and $\boldsymbol{\Phi}$ is the vector of shape functions:

$$\phi_I(\mathbf{x}) = \sum_{j=1}^{\mathrm{m}} p_j(\mathbf{x})\left(\boldsymbol{A}^{-1}(\mathbf{x})\boldsymbol{B}(\mathbf{x})\right)_{jI} \tag{12}$$

It is important to note that $u^h(\mathbf{x}_I) \neq \mathrm{u}_I$ as a consequence of the MLS interpolation, unless the prescribed data u_I is based on a polynomial function [27].

2.2. Choice of weight function

In the EFG method, the weight function $w(\mathbf{x} - \mathbf{x}_I)$ plays two major roles: i) as nodal weighting parameters, and ii) as a smoothing factor on the overall MLS function. The selection of the shape of the support domain is almost arbitrary, but a circular shape is the most convenient choice. The support radius (r_I) is used to control the limit of the 'domain of influence' and also to avoid a singularity issue of matrix $\boldsymbol{A}(\mathbf{x})$ in Equation (10), in the sense that the support domain has to be large enough to include a sufficient number of local nodes, but at the same time it needs to be as small as possible so as to preserve the locality of the influence area.

In the present approach, an exponential-based Gaussian weight function [25] is chosen which has the form:

$$w(\mathbf{x}-\mathbf{x}_I) = \begin{cases} \dfrac{\exp\left[-\left(d_I/\mathrm{c}\right)^{2\mathrm{k}}\right] - \exp\left[-\left(r_I/\mathrm{c}\right)^{2\mathrm{k}}\right]}{1-\exp\left[-\left(r_I/\mathrm{c}\right)^{2\mathrm{k}}\right]}, & 0 \le d_I \le r_I \\ 0, & d_I > r_I \end{cases} \tag{13}$$

where k and c are constants. As can be easily illustrated numerically, the parameter c is used to obtain a smooth connection between the support domain and the external area (Figure 3). In the present study, c is typically taken as $r_I / 4$ as suggested by Atluri and Zhu [26], which provides the required

smoothness condition as shown in Figure 3. Parameter k is always taken as 1 for computational simplicity.

The first derivatives of the weight function with respect to **x** (with k = 1) is thus obtained as:

$$w(\mathbf{x}-\mathbf{x}_I)_{,\mathbf{x}} = \begin{cases} -\dfrac{2d_I\left(d_{I,\mathbf{x}}\right)\cdot\exp\left[-\left(d_I/\mathrm{c}\right)^2\right]}{\mathrm{c}^2\left(1-\exp\left[-\left(r_I/\mathrm{c}\right)^2\right]\right)}, & 0\le d_I\le r_I \\ 0, & d_I > r_I \end{cases} \tag{14}$$

with subscript ",**x**" representing differentiation with respect to the spatial coordinates **x**.

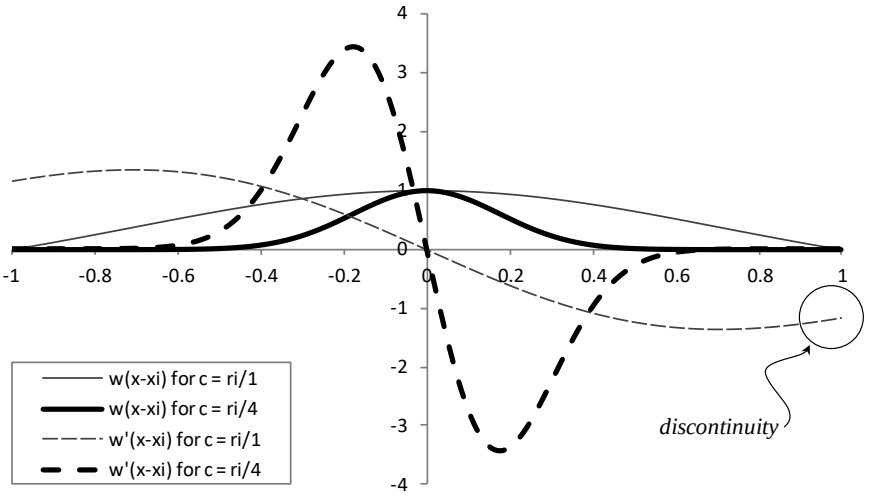

Figure 3 – Exponential weight function and its first-order derivatives for different c parameters (r_I = 1 and k = 1)

2.3. Galerkin method with MLS interpolation

Considering the displacement shape functions resulting from MLS interpolation in Equation (11), the variational weak form in Equation (4) becomes:

$$\int_\Omega \left(\boldsymbol{B}^\phi\boldsymbol{\delta u}\right)^{\mathrm{T}}\cdot\mathbf{D}\cdot\left(\boldsymbol{B}^\phi\mathbf{u}\right)\,\mathrm{d}\Omega - \int_\Omega\left(\boldsymbol{N}^\phi\boldsymbol{\delta u}\right)^{\mathrm{T}}\cdot\boldsymbol{b}\,\mathrm{d}\Omega - \int_{\Gamma_t}\left(\boldsymbol{N}^\phi\boldsymbol{\delta u}\right)^{\mathrm{T}}\cdot\boldsymbol{t}_\Gamma\,\mathrm{d}\Gamma = 0 \qquad \left(\forall\boldsymbol{\delta u}\right) \tag{15}$$

where **D** is the constitutive matrix for the plane stress case given by:

$$\mathbf{D} = \frac{\mathrm{E}t}{\left(1-\upsilon^2\right)}\begin{bmatrix} 1 & \upsilon & 0 \\ \upsilon & 1 & 0 \\ 0 & 0 & (1\text{-}\upsilon)/2 \end{bmatrix} \tag{16}$$

with E being Young's modulus, υ being Poisson's ratio and t being the plate thickness. $\boldsymbol{N}^{\phi}$ is the matrix of shape functions for the two planar displacement fields, and $\boldsymbol{B}^{\phi}$ is the strain-displacement matrix, as given by:

$$\boldsymbol{N}^{\phi} = \begin{bmatrix} \cdots & \cdots & \phi_I(\mathbf{x}) & 0 & \cdots & \cdots \\ \cdots & \cdots & 0 & \phi_I(\mathbf{x}) & \cdots & \cdots \end{bmatrix} \tag{17}$$

$$\boldsymbol{B}^{\phi} = \nabla_s \boldsymbol{N}^{\phi} = \begin{bmatrix} \cdots & \cdots & \phi_I(\mathbf{x})_{,x} & 0 & \cdots & \cdots \\ \cdots & \cdots & 0 & \phi_I(\mathbf{x})_{,y} & \cdots & \cdots \\ \cdots & \cdots & \phi_I(\mathbf{x})_{,y} & \phi_I(\mathbf{x})_{,x} & \cdots & \cdots \end{bmatrix} \tag{18}$$

Considering Equation (18), the first-order derivatives of the shape functions are obtained as:

$$\phi_I(\mathbf{x})_{,\mathbf{x}} = \boldsymbol{p}(\mathbf{x})_{,\mathbf{x}} \boldsymbol{A}(\mathbf{x})^{-1} \boldsymbol{B}(\mathbf{x}) + \boldsymbol{p}(\mathbf{x}) \left(\boldsymbol{A}(\mathbf{x})^{-1} \right)_{,\mathbf{x}} \boldsymbol{B}(\mathbf{x}) + \boldsymbol{p}(\mathbf{x}) \boldsymbol{A}(\mathbf{x})^{-1} \boldsymbol{B}(\mathbf{x})_{,\mathbf{x}} \tag{19}$$

where:

$$\left(\boldsymbol{A}(\mathbf{x})^{-1} \right)_{,\mathbf{x}} = -\boldsymbol{A}(\mathbf{x})^{-1} \left(\boldsymbol{A}(\mathbf{x}) \right)_{,\mathbf{x}} \boldsymbol{A}(\mathbf{x})^{-1} \tag{20}$$

and:

$$\left(\boldsymbol{A}(\mathbf{x}) \right)_{,\mathbf{x}} = \sum_{I=1}^{\mathrm{N}} w(\mathbf{x} - \mathbf{x}_I)_{,\mathbf{x}} \, \boldsymbol{p}^{\mathrm{T}}(\mathbf{x}_I) \boldsymbol{p}(\mathbf{x}_I) \tag{21}$$

In the above equation, $w(\mathbf{x} - \mathbf{x}_I)_{,\mathbf{x}}$ is as given by Equation (13), and $\boldsymbol{p}(\mathbf{x}_I)$ represents the monomial basis functions evaluated at $\mathbf{x}_I$. For computational efficiency, the derivatives in Equation (19) can be obtained without the explicit evaluation of the inverse of $\boldsymbol{A}(\mathbf{x})$ by applying, for example, Gaussian elimination or LU decomposition methods [28]. It is important to note that the Galerkin equation in (15) does not deal with the essential boundary conditions of Equation (2), which are addressed in the following section.

2.4. Essential boundary conditions

As previously noted, the EFG method cannot satisfy the essential boundary conditions via nodal constraints, since the MLS function does not pass through the nodal parameters, and thus the enforcement of the essential condition at the boundary nodes leads to violation of the condition on the boundary edge (e.g. $\mathbf{u} \neq \mathbf{u}_{\Gamma}$ on Γ_u). In the original EFG method by Belytschko, Lu [25], additional terms of Lagrange multipliers are employed in addressing essential boundary conditions. Such an approach comes at the cost of additional unknowns that enlarge the size of the discrete system of

equations. It was also noted to be computationally inefficient owing to the destruction of the positive definiteness of the stiffness matrix [24].

In the current method, essential boundary conditions are imposed through a penalty method, which is also often used in other numerical methods, including conventional FEM. The penalty term comprises of the following variational form:

$$-\int_{\Gamma_u} \boldsymbol{\delta}\left(\boldsymbol{u}-\boldsymbol{u}_\Gamma\right)^{\mathrm{T}} \cdot \boldsymbol{\alpha} \cdot \left(\boldsymbol{u}-\boldsymbol{u}_\Gamma\right)\ \mathrm{d}\Gamma = 0 \qquad \left(\forall \boldsymbol{\delta u}\right) \tag{22}$$

where $\boldsymbol{\alpha}$ is a diagonal matrix of penalty factors (α_x, α_y) and ($\boldsymbol{u} - \boldsymbol{u}_\Gamma$) is the residual condition to be penalised so that $\boldsymbol{u} \approx \boldsymbol{u}_\Gamma$ along the boundary with essential conditions. This method does not enforce the given condition fully unless a very large penalty terms are used for $\boldsymbol{\alpha}$, though the specific choice should be made with great care to avoid numerical problems arising from ill-conditioning. Liu [24] suggested that the value of $\boldsymbol{\alpha}$ should be between 10^4 and 10^{13} multiplied by the maximum of the diagonal terms in the stiffness matrix.

Considering the penalty term, the updated form of Equation (15) can be written as :

$$\begin{aligned}
&\int_\Omega \left(\boldsymbol{B}^\phi \boldsymbol{\delta u}\right)^{\mathrm{T}} \cdot \mathbf{D} \cdot \left(\boldsymbol{B}^\phi \mathbf{u}\right)\ \mathrm{d}\Omega - \int_\Omega \left(\boldsymbol{N}^\phi \boldsymbol{\delta u}\right)^{\mathrm{T}} \cdot \boldsymbol{b}\ \mathrm{d}\Omega - \int_{\Gamma_t} \left(\boldsymbol{N}^\phi \boldsymbol{\delta u}\right)^{\mathrm{T}} \cdot \boldsymbol{t}_\Gamma\ \mathrm{d}\Gamma - \cdots \\
&\int_{\Gamma_u} \left(\boldsymbol{N}^\phi \boldsymbol{\delta u}\right)^{\mathrm{T}} \cdot \boldsymbol{\alpha} \cdot \left(\boldsymbol{N}^\phi \mathbf{u}\right)\ \mathrm{d}\Gamma + \int_{\Gamma_u} \left(\boldsymbol{N}^\phi \boldsymbol{\delta u}\right)^{\mathrm{T}} \cdot \boldsymbol{\alpha} \cdot \boldsymbol{u}_\Gamma\ \mathrm{d}\Gamma = 0 \qquad \left(\forall \boldsymbol{\delta u}\right)
\end{aligned} \tag{23}$$

or in a more generalised form of discrete linear equations:

$$\left(\int_\Omega \boldsymbol{B}^{\phi\mathrm{T}} \mathbf{D} \boldsymbol{B}^\phi \mathrm{d}\Omega + \int_{\Gamma_u} \boldsymbol{\psi}^{\mathrm{T}} \boldsymbol{\alpha} \boldsymbol{\psi}\ \mathrm{d}\Gamma\right)\mathbf{u} = \int_{\Gamma_t} \boldsymbol{N}^{\phi\mathrm{T}} \boldsymbol{t}_\Gamma\ \mathrm{d}\Gamma + \int_\Omega \boldsymbol{N}^{\phi\mathrm{T}} \boldsymbol{b}\ \mathrm{d}\Omega + \int_{\Gamma_u} \boldsymbol{N}^{\phi\mathrm{T}} \boldsymbol{\alpha} \boldsymbol{u}_\Gamma\ \mathrm{d}\Gamma \qquad \left(\forall \boldsymbol{\delta u}\right) \tag{24}$$

This can be symbolised in terms of stiffness matrix (**k**), penalty stiffness matrix ($\mathbf{k}^\alpha$), displacements vector (**u**) and an equivalent loading vector (**f**) to yield the following form:

$$\left[\mathbf{k} + \mathbf{k}^\alpha\right]\mathbf{u} = \mathbf{f} \tag{25}$$

where the associated terms are defined as:

$$\begin{aligned}
\mathbf{k}_{IJ} &= \int_\Omega \boldsymbol{B}_I^{\phi\mathrm{T}} \mathbf{D} \boldsymbol{B}_J^\phi\ \mathrm{d}\Omega \\
\mathbf{k}_{IJ}^\alpha &= \int_{\Gamma_u} \boldsymbol{\psi}_I{}^{\mathrm{T}} \boldsymbol{\alpha} \boldsymbol{\psi}_J\ \mathrm{d}\Gamma \\
\mathbf{f}_I &= \int_{\Gamma_t} \boldsymbol{N}^{\phi\mathrm{T}} \boldsymbol{t}_\Gamma\ \mathrm{d}\Gamma + \int_\Omega \boldsymbol{N}^{\phi\mathrm{T}} \boldsymbol{b}\ \mathrm{d}\Omega + \int_{\Gamma_u} \boldsymbol{N}^{\phi\mathrm{T}} \boldsymbol{\alpha} \boldsymbol{u}_\Gamma\ \mathrm{d}\Gamma
\end{aligned} \tag{26}$$

with the components of $\mathbf{k}_{IJ}^{\alpha}$ defined as:

$$\boldsymbol{\psi}_I = \begin{bmatrix} \phi_I(\mathbf{x}) & 0 \\ 0 & \phi_I(\mathbf{x}) \end{bmatrix} \quad , \quad \boldsymbol{\alpha} = \begin{bmatrix} \alpha_x & 0 \\ 0 & \alpha_y \end{bmatrix} \tag{27}$$

2.5. Background cells for integration

One of the issues relating to the application of the EFG method is the need for background cells for numerical integration, as a result of which the method is claimed to be not a 'truly meshless' method [26]. Nevertheless, the application of such a background 'mesh' for integration is much more flexible than the FEM due to the fact that the cells are only utilised for numerical integration, thus a simple grid of rectangular shapes would be satisfactory.

An important issue arising with the EFG method relates to integration over irregular domains, since a simple rectangular grid without modifications cannot perfectly fit a domain with curved boundary. Belytschko, Lu [25] proposed that irregular domains can be performed by ignoring all Gauss points outside the domain during the summation. This basically considers the domain integrand function to retain its values within the domain Ω but become zero outside Ω. Due to the discontinuity introduced in the function within the integration cells across the boundary, inaccuracy in the integration could occur if limited quadrature points are used. More advanced methods include the adoption of triangulation integration schemes to fit an irregular domain as presented in [29, 30], particularly in the context of moving discontinuities as in the modelling of evolving cracks. Such methods require a more complex algorithm, including the modification of quadrature weights, so as to deal with an arbitrary integration domain that changes with crack growth.

In this work, a simple and accurate approach for a planar analysis problem is proposed based on a multi-level rectangular grid (MLRG), in which the cells that intersect the boundary are hierarchically reduced in size (e.g. by dividing the original cell side into two). Ultimately, the cells that lie outside the boundary are not considered, as illustrated in Figure 4. This is nothing more than preventing Gauss points from falling outside the domain so that no elimination of Gauss points has to take place. Despite having a concentration of quadrature points near the curved boundary, it is shown later that this technique is quite efficient, as only a small number of quadrature points per cell is required whilst preserving the simplicity of having background cells based on a rectangular grid.

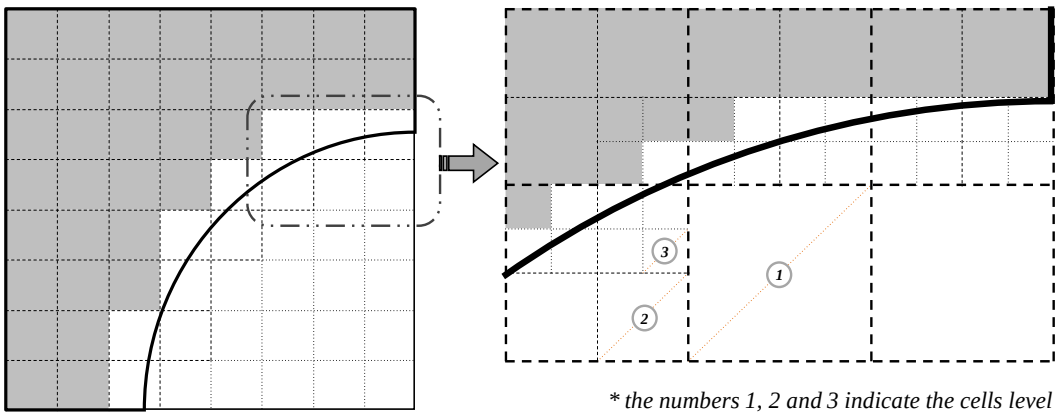

Figure 4 – Numerical integration for irregular domain with two hierarchic subdivisions

Numerical integration in this study is performed using a Gaussian quadrature scheme via a set of rectangular background cells. In each cell, $N_g \times N_g$ Gauss quadrature points ($\mathbf{x}_q$) are employed, which makes the total number of Gauss points in the domain $M_\Omega = N_c \times N_g^{\,2}$, where N_c is the number of cells. With regard to line integration, such as over the boundary, this is performed by partitioning the line into N_L segments, each of which containing 9 quadrature points, hence $M_\Gamma = 9 \times N_L$. Having determined the location of Gauss points ($\mathbf{x}_q$), their weights (w_q) and the corresponding Jacobian (J^e), the components in Equation (26) can be obtained using Gaussian quadrature as:

$$
\begin{aligned}
\mathbf{k}_{IJ} &= \sum_{q=1}^{M_\Omega} w_q \; \boldsymbol{B}_I^{\phi \mathrm{T}}(\mathbf{x}_q)\mathbf{D}\boldsymbol{B}_J^{\phi}(\mathbf{x}_q) \; J^e \\
\mathbf{k}_{IJ}^{\alpha} &= \sum_{q=1}^{M_\Omega} w_q \; \boldsymbol{\psi}_I{}^{\mathrm{T}}(\mathbf{x}_q)\boldsymbol{\alpha}\boldsymbol{\psi}_J(\mathbf{x}_q) \; J^e \\
\mathbf{f}_I &= \sum_{q=1}^{M_\Gamma} w_q \; \boldsymbol{N}_I^{\phi \mathrm{T}}(\mathbf{x}_q)\boldsymbol{t}_\Gamma \; J^e \; + \sum_{q=1}^{M_\Gamma} w_q \boldsymbol{N}_I^{\phi \mathrm{T}}(\mathbf{x}_q)\boldsymbol{b} \; J^e \; + \sum_{q=1}^{M_\Gamma} w_q \boldsymbol{N}_I^{\phi \mathrm{T}}(\mathbf{x}_q)\boldsymbol{\alpha}\boldsymbol{u}_\Gamma \; J^e
\end{aligned}
\tag{28}
$$

where $\mathbf{k}_{IJ}$ is the 2×2 matrix component of the full 2N×2N matrix $\mathbf{k}$, and the same applies to $\mathbf{k}_{ij}^{\alpha}$. $\boldsymbol{N}_I^{\phi}(\mathbf{x}_q)$ and $\boldsymbol{B}_I^{\phi}(\mathbf{x}_q)$ are, respectively, the shape function and strain-displacement matrices of node I evaluated at Gauss points $\mathbf{x}_q$. The term $\boldsymbol{\psi}_I(\mathbf{x}_q)$ is also a matrix of shape functions which is given by Equation (27).

3. Unit-Cell Formulation

The planar response for a cellular beam is assembled from contributions of super-elements, each representing the characteristic response of a unit-cell. The formulation of the unit-cell super-

element, its contribution to the global cellular beam response, and the recovery of the planar stresses after determination of the super-element nodal parameters are presented hereafter.

3.1. Unit-cell level

A unit-cell refers to a portion between two adjacent openings of a cellular beam or between an opening and the beam end, as previously illustrated in Figure 2. The unit-cell response is approximated by means of a super-element utilising three DOF (u_i v_i θ_i) at the tee centroids, corresponding to four 'super-element nodes' for a single super-element. As for the outer edges of the end cells, the cross-section of the top and bottom tees extends to include web areas up to mid-depth of the cell. As shown in Figure 5, the associated components of internal forces, horizontal force fx_i, vertical force fy_i and moment m_i, are used to establish the characteristic super-element response as discussed later, and minimum restraint of rigid body movement is applied at three locations along the mid-depth of the web-post. The unit cell is considered for illustrative purposes under the action of a uniformly distributed load (UDL) q acting along the top edge, which allows a step-wise distributed load over the full beam span, though more sophisticated load distributions can also be easily considered in the proposed approach.

Where the cellular beam is subject to sagging bending moment under applied loading, the top and bottom flanges are affected by compressive and tensile stresses, respectively. Provided the flanges are relatively narrow, shear lag effects may be ignored [31], and thus a plane stress idealisation may be reasonably assumed for the web as well as flange regions. This allows the planar response to be modelled using a 2D model in which the web and flange regions have different out-of-plane thicknesses, where the thickness for the flanges is taken equal to their width. The issue concerning material discontinuity between the web and flange components, as pointed by Liu [24], can lead to discontinuity in the transverse normal stress σ_{yy} and shear stress τ_{xy}, though this can still be approximated well with continuous MLS functions subject to adequate transverse discretisation at these locations.

The applied tractions of fx_i, fy_i and m_i along the side edges account for changes in the thickness, as demonstrated in Figure 6. In the analysis, anti-clockwise moments are considered positive, and the action of vertical shear in the tee section is assumed to be effective only along the web area, which is realistic for relatively thin flanges.

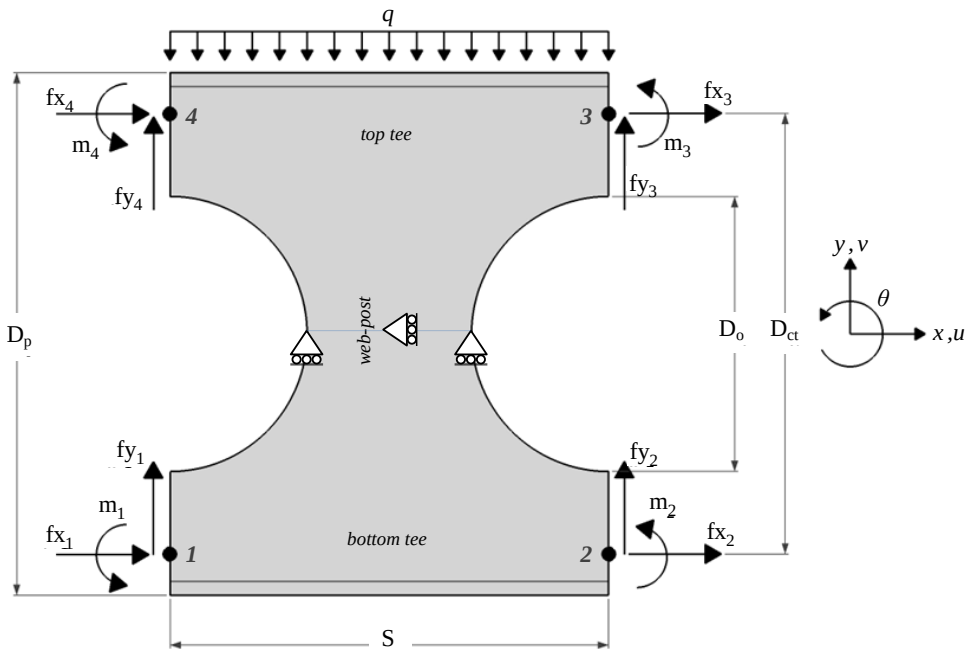

Figure 5 – Unit cell under representative actions

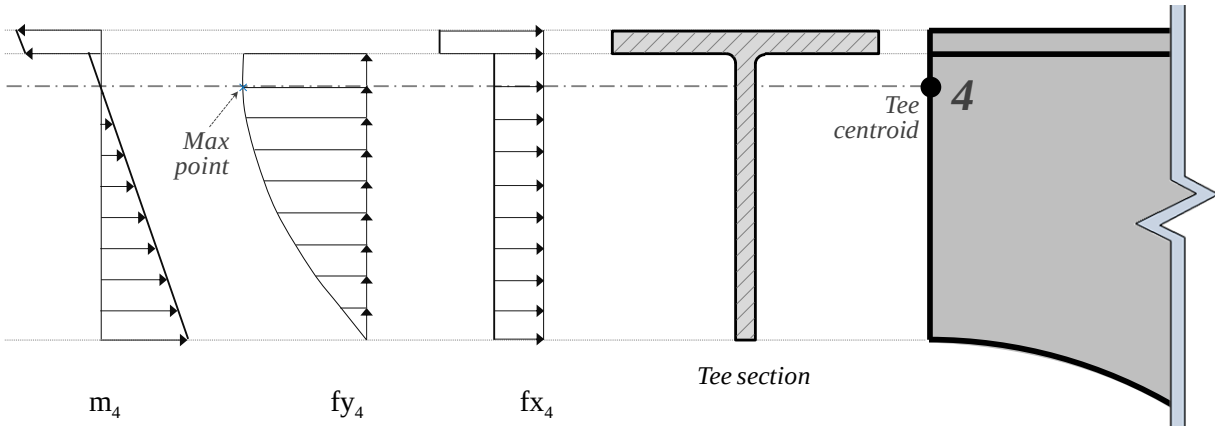

Figure 6 – Unit cell tractions on boundary Γ_4

3.2. Representative actions

In establishing the overall planar response of a cellular beam, typical cell configurations are subjected to EFG discretisation and considered under representative actions to establish their characteristic super-element response, and standard assembly procedures are then employed to obtain the discrete response of the overall cellular beam. The characteristic unit cell response is determined on the basis of a flexibility-based formulation, by considering alternative load cases of unit tractions,

each corresponding to one of the super-element DOF nodes 2 to 4, while equilibrium of the unit cell is satisfied by similar tractions at node 1 (Figure 5).

A brief formulation of the representative actions is presented here. Consider a unit cell (Figure 5) as a super-element possessing 12 DOF defined by:

$$\begin{aligned} \mathbf{U_A} &= \langle u_1,\, v_1,\, \theta_1 \rangle^{\mathrm{T}} \quad \text{for node 1} \\ \mathbf{U_B} &= \langle u_2,\, v_2,\, \theta_2,\, u_3,\, v_3,\, \theta_3,\, u_4,\, v_4,\, \theta_4 \rangle^{\mathrm{T}} \quad \text{for node 2, 3 and 4} \end{aligned} \tag{29}$$

The associated components of forces, $\mathbf{P_A}$ and $\mathbf{P_B}$, are defined as

$$\begin{aligned} \mathbf{P_A} &= \langle fx_1,\, fy_1,\, m_1 \rangle^{\mathrm{T}} \quad \text{for node 1} \\ \mathbf{P_B} &= \langle fx_2,\, fy_2,\, m_2,\, fx_3,\, fy_3,\, m_3,\, fx_4,\, fy_4,\, m_4 \rangle^{\mathrm{T}} \quad \text{for node 2, 3 and 4} \end{aligned} \tag{30}$$

The effect of a unit force, for example horizontal force at node 2, is studied by applying a unit traction at that particular point, $fx_2 \equiv \int_{\Gamma_2} \boldsymbol{\sigma}_{x2}\, d\Gamma = 1$, while equilibrating the system with additional equivalent forces at node 1, $fx_1 = -1$ and $fy_1 = m_1 = 0$, so as to avoid reactions and hence stress concentrations at the web-post supports, as illustrated in Figure 7. Based on the principle of virtual work along the boundary of node 2 (Γ_2), the nodal displacement u_2 associated with the applied forces can be determined by

$$u_2 \cdot fx_2 = \int_{\Gamma_2} \boldsymbol{\sigma}_{x2}{}^{\mathrm{T}} \boldsymbol{u}_{x2}\, d\Gamma \quad \overset{fx_2=1}{\Rightarrow} \quad u_2 = \int_{\Gamma_2} \boldsymbol{\sigma}_{x2}{}^{\mathrm{T}} \boldsymbol{u}_{x2}\, d\Gamma \tag{31}$$

where $\boldsymbol{u}_{x2}$ is the vector of horizontal displacements for all points along Γ_2. This is where meshfree method is of benefit since the recovery of $\boldsymbol{\sigma}_{x2}$ and $\boldsymbol{u}_{x2}$ values along Γ_2 (at the Gauss points) is very straightforward due to the continuous approximated field by the MLS shape function.

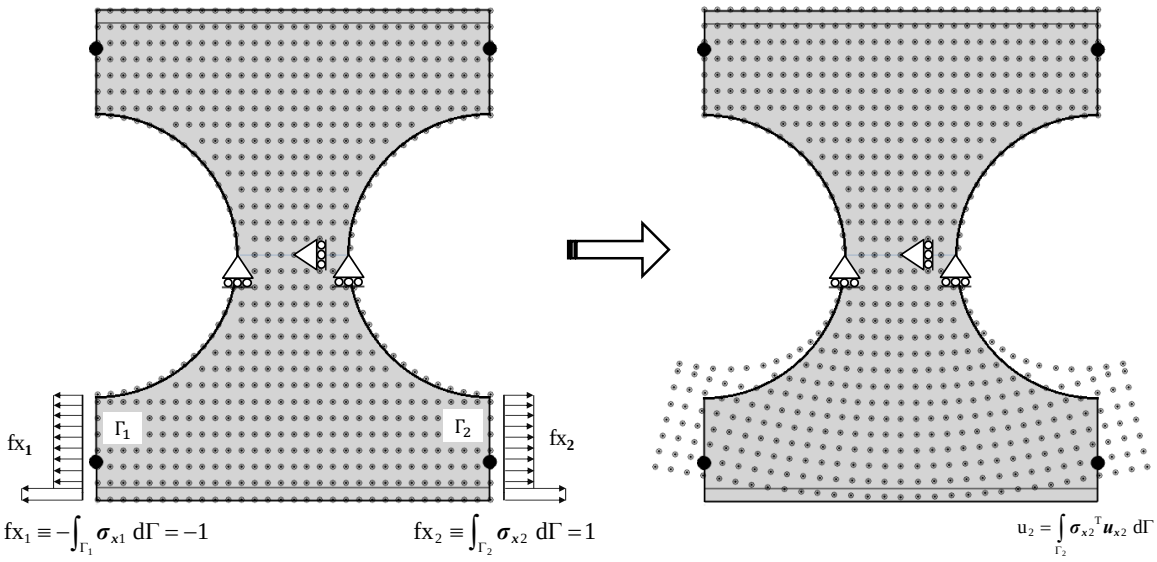

Figure 7 – Effect of a unit horizontal force at Node 2 and the equilibrating force at Node 1

With each load case associated with a set of nodal displacements in accordance with the EFG approximation, this provides a flexibility matrix which can be inverted for the planar stiffness matrix of the 4-noded super-element representing the individual unit cell response. Note that displacement compatibility along the edges between adjacent unit cell super-elements is satisfied only in an approximate weak sense, as can be observed for example from Equation (31) where the same u_2 does not guarantee the same $\boldsymbol{u}_{x2}$ along the whole edge. Accordingly, a model for the whole beam based on the assembly of super-element contributions is expected to be associated with some compatibility defaults which can lead to a more flexible response compared to a full 2D model of the overall beam. However, as shown in subsequent application examples, the proposed unit-cell approach combines computational efficiency arising from the super-element simplification with high levels of solution accuracy.

The full expression of the flexibility formulation can be written as:

$$\begin{Bmatrix} \mathbf{U_A} \\ \cdots \\ \mathbf{U_B} \end{Bmatrix} = \underbrace{\begin{bmatrix} \mathbf{F_A} \\ \cdots \\ \mathbf{F_B} \end{bmatrix}}_{12\times 9} \mathbf{P_B} + q \begin{Bmatrix} \mathbf{u_{qA}} \\ \cdots \\ \mathbf{u_{qB}} \end{Bmatrix} + \underbrace{\begin{bmatrix} \mathbf{I}_{3\times 3} \\ \cdots \\ \mathbf{T_B} \end{bmatrix}}_{12\times 3} \overline{\mathbf{U}}_{\mathbf{A}} \tag{32}$$

in which $[\mathbf{F_A}, \mathbf{F_B}]^{\mathrm{T}}$ is the flexibility matrix obtained by separate analyses of the unit cell under specific traction forces in $\mathbf{P_B}$. The effect of uniform-distributed loads, q, is accounted for in the equation by the component $\langle \mathbf{u_{qA}},\ \mathbf{u_{qB}} \rangle^{\mathrm{T}}$ that is the flexibility vector associated with q. The vector $\overline{\mathbf{U}}_A = \langle \bar{u}_1,\ \bar{v}_1,\ \bar{\theta}_1 \rangle^{\mathrm{T}}$

corresponds to additional displacements at node 1 which allow for rigid body movement, where $\mathbf{I}_{3\times3}$ is a 3×3 identity matrix, and $\mathbf{T_B}$ is a rigid body transformation matrix given by:

$$\mathbf{T_B} = \left[\begin{array}{ccc|ccc|ccc} 1 & 0 & 0 & 1 & 0 & 0 & 1 & 0 & 0 \\ 0 & 1 & 0 & 0 & 1 & 0 & 0 & 1 & 0 \\ 0 & S & 1 & -D_{ct} & S & 1 & -D_{ct} & 0 & 1 \end{array}\right]^T \tag{33}$$

in which S and D_{ct} denote the horizontal and vertical distances between the super-element nodes (Figure 5). Equilibrium conditions are also used to relate $\mathbf{P_A}$ to $\mathbf{P_B}$ and q as follows:

$$\mathbf{P_A} = -\mathbf{T_B}^T \cdot \mathbf{P_B} + q\ \mathbf{T_q} \tag{34}$$

where $\mathbf{T_q} = \left\langle 0,\ S,\ S^2/2 \right\rangle^T$.

The flexibility Equation (32) can now be converted to a stiffness-based formulation, by solving for $\mathbf{P_B}$ and eliminating $\overline{\mathbf{U}}_\mathbf{A}$ as follows:

$$\begin{aligned}
&\underbrace{\begin{bmatrix} \mathbf{F_A} \\ \cdots \\ \mathbf{F_B} \end{bmatrix}}_{12\times9} \mathbf{P_B} = \begin{Bmatrix} \mathbf{U_A} \\ \cdots \\ \mathbf{U_B} \end{Bmatrix} - q \begin{Bmatrix} \mathbf{u_{qA}} \\ \cdots \\ \mathbf{u_{qB}} \end{Bmatrix} - \underbrace{\begin{bmatrix} \mathbf{I}_{3\times3} \\ \cdots \\ \mathbf{T_B} \end{bmatrix}}_{12\times3} \overline{\mathbf{U}}_\mathbf{A} \Rightarrow \\
&\overbrace{\underbrace{\left[-\mathbf{T_B} \vdots \mathbf{I}_{9\times9}\right]}_{9\times12} \underbrace{\begin{bmatrix} \mathbf{F_A} \\ \cdots \\ \mathbf{F_B} \end{bmatrix}}_{12\times9}}^{\mathbf{F}} \mathbf{P_B} = \underbrace{\left[-\mathbf{T_B} \vdots \mathbf{I}_{9\times9}\right]}_{9\times12} \begin{Bmatrix} \mathbf{U_A} \\ \cdots \\ \mathbf{U_B} \end{Bmatrix} - q \underbrace{\left[-\mathbf{T_B} \vdots \mathbf{I}_{9\times9}\right]}_{9\times12} \begin{Bmatrix} \mathbf{u_{qA}} \\ \cdots \\ \mathbf{u_{qB}} \end{Bmatrix} \Rightarrow \\
&\mathbf{P_B} = \mathbf{F}^{-1} \underbrace{\left[-\mathbf{T_B} \vdots \mathbf{I}_{9\times9}\right]}_{9\times12} \begin{Bmatrix} \mathbf{U_A} \\ \cdots \\ \mathbf{U_B} \end{Bmatrix} - q\ \mathbf{F}^{-1} \underbrace{\left[-\mathbf{T_B} \vdots \mathbf{I}_{9\times9}\right]}_{9\times12} \begin{Bmatrix} \mathbf{u_{qA}} \\ \cdots \\ \mathbf{u_{qB}} \end{Bmatrix}
\end{aligned} \tag{35}$$

Considering Equation (34), this expression can be extended to include the resistance forces at all four super-element nodes:

$$\begin{Bmatrix}\mathbf{P_A}\\ \cdots\\ \mathbf{P_B}\end{Bmatrix}=\underbrace{\begin{bmatrix}-\mathbf{T_B}\\ \cdots\\ \mathbf{I}_{9\times9}\end{bmatrix}}_{12\times9}\overbrace{\left(\mathbf{F}^{-1}\underbrace{\left[-\mathbf{T_B}\ \vdots\ \mathbf{I}_{9\times9}\right]}_{9\times12}\begin{Bmatrix}\mathbf{U_A}\\ \cdots\\ \mathbf{U_B}\end{Bmatrix}-q\,\mathbf{F}^{-1}\underbrace{\left[-\mathbf{T_B}\ \vdots\ \mathbf{I}_{9\times9}\right]}_{9\times12}\begin{Bmatrix}\mathbf{u_{qA}}\\ \cdots\\ \mathbf{u_{qB}}\end{Bmatrix}\right)}^{\mathbf{P_B}}+q\begin{Bmatrix}\mathbf{T_q}\\ \cdots\\ \mathbf{0}_{9\times1}\end{Bmatrix}$$

$$\overbrace{\begin{Bmatrix}\mathbf{P}_A\\ \cdots\\ \mathbf{P}_B\end{Bmatrix}}^{\mathbf{P^E}}=\overbrace{\underbrace{\begin{bmatrix}-\mathbf{T_B}\\ \cdots\\ \mathbf{I}_{9\times9}\end{bmatrix}}_{12\times9}\left[\mathbf{F}\right]^{-1}\underbrace{\left[-\mathbf{T_B}\ \vdots\ \mathbf{I}_{9\times9}\right]}_{9\times12}}^{\mathbf{K^E}}\overbrace{\begin{Bmatrix}\mathbf{U_A}\\ \cdots\\ \mathbf{U_B}\end{Bmatrix}}^{\mathbf{U^E}}-\overbrace{q\left(\mathbf{K^E}\begin{Bmatrix}\mathbf{u_{qA}}\\ \cdots\\ \mathbf{u_{qB}}\end{Bmatrix}-\begin{Bmatrix}\mathbf{T_q}\\ \cdots\\ \mathbf{0}_{9\times1}\end{Bmatrix}\right)}^{\mathbf{P_p^E}} \tag{36}$$

$$\mathbf{P^E}=\mathbf{K^E}\cdot\mathbf{U^E}-\mathbf{P_p^E}$$

This is the final expression for the unit-cell super-element response, which is characteristic of a linear discrete system. The above expression needs to be evaluated only once for identical unit cells which are repeated along a cellular beam, where the overall beam response can then be assembled without an undue increase in computational cost. Note that $\mathbf{K^E}$ is a symmetric matrix, and hence the overall stiffness matrix, which is simply the assembly of the individual unit stiffness matrices $\mathbf{K^E}$, is also a symmetric matrix. In addition, the overall stiffness matrix could be banded with appropriate numbering of the super-element nodes.

3.3. Global analysis

The global stiffness matrix is obtained by assembling the stiffness matrices of individual super-elements, and the linear system of equilibrium equations is solved using standard techniques allowing for essential boundary conditions at the super-element nodes. The set of linear equations associated with the global system is given by:

$$\mathbf{K^G U^G = P^G + P_p^G}\quad\Rightarrow\mathbf{U^G}=\left(\mathbf{K^G}\right)^{-1}\left(\mathbf{P^G + P_p^G}\right) \tag{37}$$

where $\mathbf{K^G}$ is the global stiffness matrix of size $3N_e\times3N_e$, N_e being the number of super-element nodes, and:

$$\begin{aligned}\mathbf{U^G}&=\left\langle U_1,\ V_1,\ \Theta_1,\ U_2,\ V_2,\ \Theta_2,\cdots,\ U_{N_e},\ V_{N_e},\ \Theta_{N_e}\right\rangle^{\mathrm{T}}\\ \mathbf{P^G}&=\left\langle Fx_1,\ Fy_1,\ M_1,\ Fx_2,\ Fy_2,\ M_2,\cdots,\ Fx_{N_e},\ Fy_{N_e},\ M_{N_e}\right\rangle^{\mathrm{T}}\end{aligned} \tag{38}$$

$\mathbf{P_p^G}$ is a vector of equivalent global nodal loads corresponding to distributed loading q, which has the form:

$$\mathbf{P}_{\mathbf{p}}^{\mathbf{G}} = \left\langle \left\langle \mathbf{P}_{\mathbf{p}}^{\mathbf{E}} \right\rangle_1, \left\langle \mathbf{P}_{\mathbf{p}}^{\mathbf{E}} \right\rangle_2, \cdots, \left\langle \mathbf{P}_{\mathbf{p}}^{\mathbf{E}} \right\rangle_{\mathrm{N_e}} \right\rangle^{\mathrm{T}} \tag{39}$$

where $\left\langle \mathbf{P}_{\mathbf{p}}^{\mathbf{E}} \right\rangle_i = \left\{ \mathbf{P}_{\mathbf{p}}^{\mathbf{E}} \right\}_i^{\mathrm{T}}$ is the local components vector obtained in Equation (36):

$$\left\{ \mathbf{P}_{\mathbf{p}}^{\mathbf{E}} \right\}_i = q \left(\mathbf{K}^{\mathbf{E}} \begin{Bmatrix} \mathbf{u}_{\mathbf{qA}} \\ \cdots \\ \mathbf{u}_{\mathbf{qB}} \end{Bmatrix} - \begin{Bmatrix} \mathbf{T}_{\mathbf{q}} \\ \cdots \\ \mathbf{0}_{9\times 1} \end{Bmatrix} \right) \tag{40}$$

Having obtained the global displacements $\mathbf{U}^{\mathbf{G}}$ from Equation (37), local reactions of the modular unit cells at each super-node can be readily determined, which in turn enable the recovery of planar stresses, as discussed hereafter.

3.4. Recovery of planar stresses over unit-cell

The following expression summarises the determination of the planar stress field of the current approach:

$$\boldsymbol{\sigma}_j = \begin{Bmatrix} \sigma_x \\ \sigma_y \\ \tau_{xy} \end{Bmatrix}_j = \mathbf{D}\boldsymbol{\varepsilon}_j = \mathbf{D}\boldsymbol{B}_j \overbrace{\left(\begin{bmatrix} \mathbf{F}_{\mathbf{B}} \vdots \mathbf{u}_{\mathbf{qB}} \end{bmatrix} \begin{Bmatrix} \mathbf{P}_{\mathbf{B}} \\ \cdots \\ q \end{Bmatrix} \right)}^{\mathbf{u}_I} \tag{41}$$

in which $\mathbf{D}$ is the plane stress constitutive matrix, and $\boldsymbol{B}_j$ is the strain displacement matrix where subscript j is the index for Gauss points in unit cells. The terms in bracket produce the planar displacements vector $\mathbf{u}_I$ of nodes in the super-element domain, where $\begin{bmatrix} \mathbf{F}_{\mathbf{B}} \vdots \mathbf{u}_{\mathbf{qB}} \end{bmatrix}$ is a transformation matrix relating the EFG nodal parameters to the discrete forces of the super-element nodes $\mathbf{P}_{\mathbf{B}}$ and distributed load q. This equation encapsulates the two levels of discretisation employed for planar analysis, namely the EFG and super-element levels.

It is important to note that since a unit-based analysis of the full beam is implemented, the obtained stresses are continuous only within the local cell domain, though the associated inaccuracy is negligible for typical beams, as illustrated later in the verification examples. Moreover, a continuous field of the planar stress could be achieved by applying the MLS approximation at the overall beam level, though the computational effort would then be relatively excessive. Indeed, the proposal of unit-cell super-elements in this work is primarily aimed at overcoming this excessive computational demand while retaining good levels of accuracy in the planar stress distribution.

3.5. Overall Numerical Procedure

A numerical procedure for planar analysis of a whole cellular beam using the proposed EFG method is illustrated in Figure 8. The calculation involves two different levels of analysis, namely the global beam and local unit-cell levels. For a regular cellular beam subjected to a UDL on top of its flange, only three unit-cells, left end, right end and internal cell, need to be analysed locally by the EFG method. Each unit-cell is then considered as a super-element, where the internal super-element is repeatedly applied as a modular computational entity for the various internal cells along the span. The significant advantages of this approach in terms of accuracy and computational efficiency are highlighted through several illustrative examples presented in the subsequent sections.

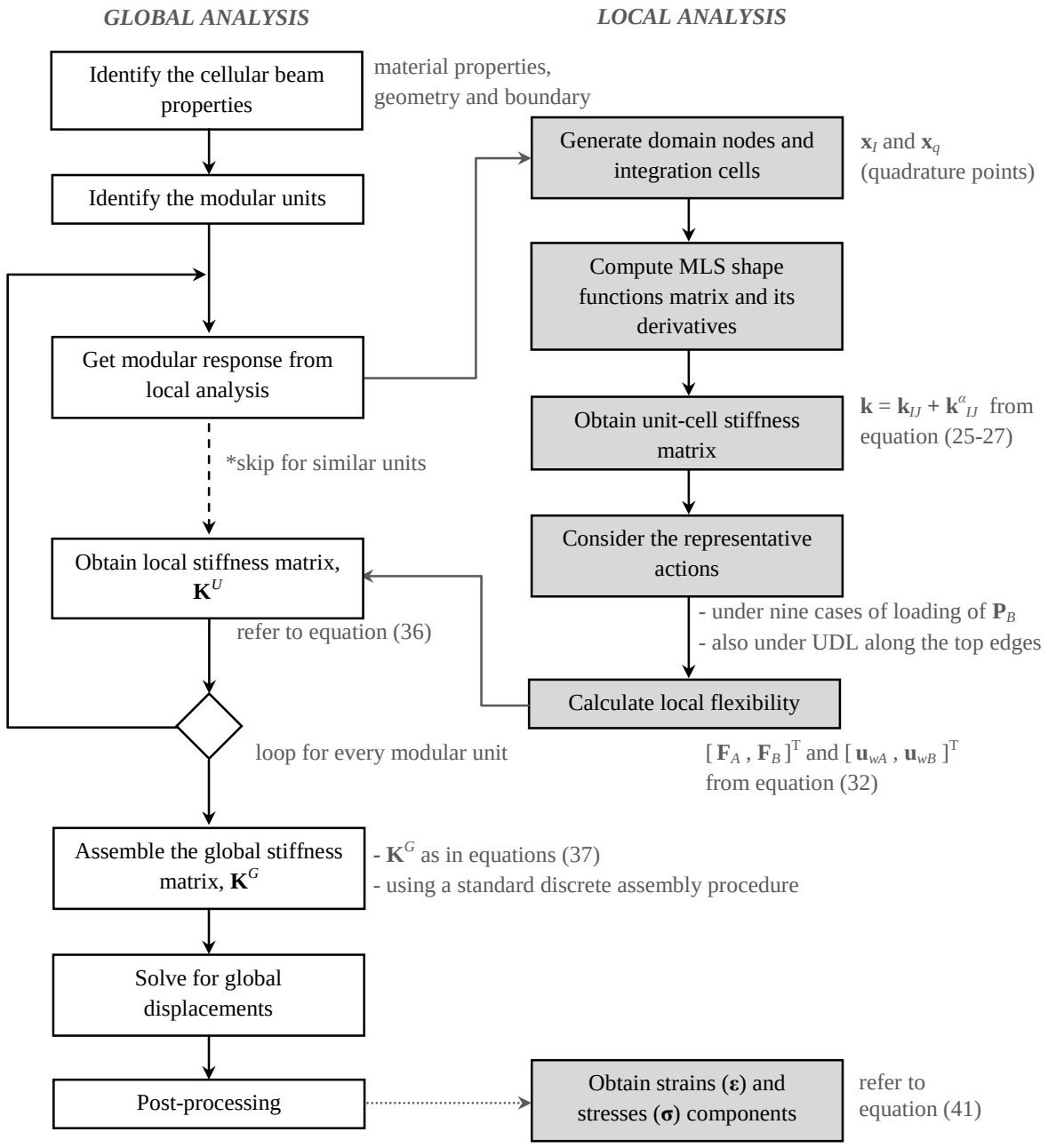

Figure 8 – Flowchart of the proposed EFG method for cellular beams planar analysis

4. Numerical Examples and Discussion

Here, numerical examples are presented to evaluate the performance of the developed EFG method considering the MLRG integration approach for the planar analysis of the web panel in a unit-cell (without the flanges). Two specific cases are chosen to examine the ability of the EFG method in dealing with irregular domains under general loading conditions.

The selection of support radius and domain integration parameters is discussed. As suggested earlier, parameters in the weight function of Equation (13) are kept as k = 1 and c = r_I/ 4 in all calculations, unless stated otherwise. A quadratic basis function is used herein. Discretisation over the domain is made on the basis of a rectangular grid (as close to square as possible), where the EFG nodes are located at all grid intersections within the domain, and additional nodes are introduced along curved edges. Another layer consisting of a different rectangular grid is also employed for numerical integration. These two sets of grid could be of the same formation, but for generality they are allowed to be different. This is to enable a complete order integration rule to be employed with a coarse discretisation of the displacement fields.

For the two considered examples, the MLS approximation employs quadratic basis functions. Comparison is made between the developed EFG method and detailed FEA models, where relative performance is investigated in relation to the total DOFs. Since a theoretical solution is not available for these problems, the 'exact' solution is estimated from a detailed FEA model with a very fine mesh.

4.1. Unit cell under transverse compressive load

As illustrated in Figure 9, a unit cell of a cellular beam with a depth D_p = 1.0 m, hole diameter D_o = 0.6 m, spacing S = 0.8m and web thickness t_w = 0.001 m is considered for the first case. The panel is loaded with 1kN/m UDL along the top and the bottom edges in opposite directions to cause significant compression, where the material parameters are E = 210×10^9 N/m^2 and υ = 0.25. As mentioned earlier, the three nodal supports across the web-post are used to prevent rigid body movement.

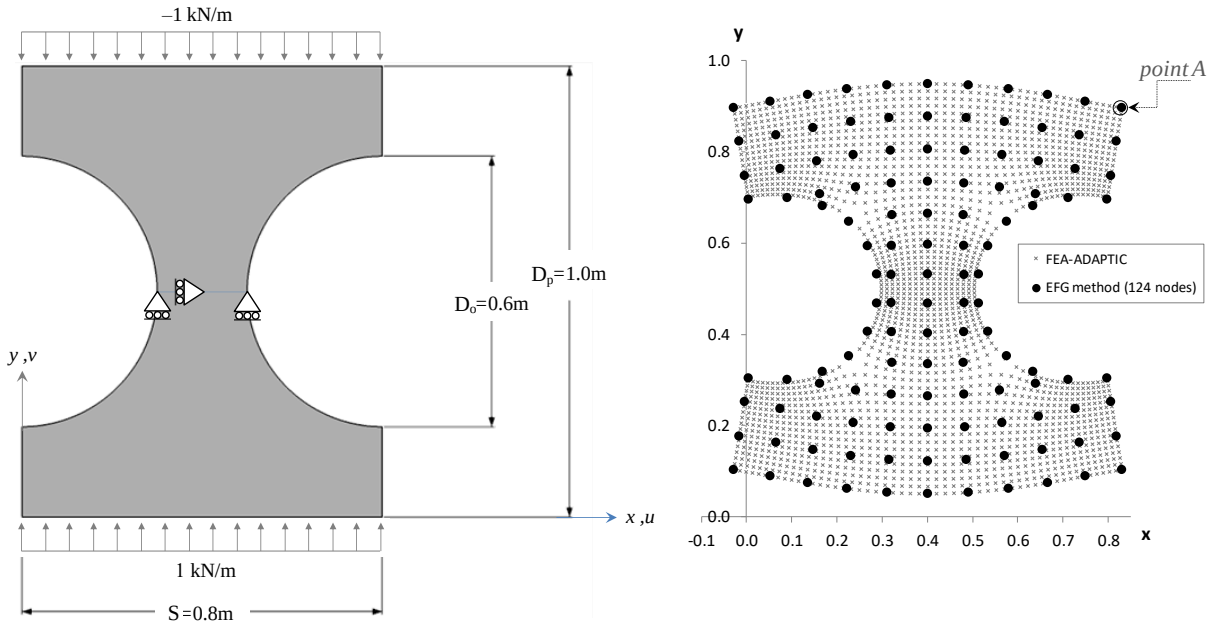

Figure 9 – Unit cell under transverse compression: (a) applied loads and boundary conditions, (b) distribution of nodes and deflected shapes with EFG and FEA models

As can be seen, the domain discretisation of the panel using the EFG method is performed using a rectangular grid of nodes, excluding nodes that would be located outside the domain boundary. Additional nodes are employed along the curved edges (Figure 9(b)) in order to improve the accuracy of the MLS approximation functions.

Figure 9(b) shows the deflected shape of a unit cell under transverse compression, comparing the EFG prediction with the FEA result. In the following discussion, the vertical displacement of point A (u_A) is used as a reference, and where appropriate reference to the strain energy (e) of the system is also considered. From a detailed finite element analysis performed using ADAPTIC, the estimated exact solution for this problem is: $u_A = -1.0343\times10^{-5}$ m and e = 5.6945N.m.

4.1.1. Influence of support radius

The effect of the support radius r_I is conducted here for the irregular domain, where irregularity in the nodal distribution occurs near the curved edges. Two cases considering different sets of nodes (a) 124 nodes based on a rectangular grid of 10×13, and (b) 392 nodes based on a 20×25 grid, are used in conjunction with 3×3 or 6×6 quadrature within a sufficient number of rectangular background cells, as elaborated in Section 4.1.2. Results are summarised in Figure 10(a) and (b) for

the normalised displacement and strain energy in terms of $\kappa = r_I / \mathrm{h}$, where h is the nodal spacing, taken as the maximum of the two element edge lengths in the x and y directions. It is observed that for κ exceeding 6.0, the deflection prediction deteriorates for the two levels of discretisation, while for κ less than 4.0 the strain energy tends to be underestimated. On the other hand, the use of different quadrature rules has a relatively a small effect. Accordingly, r_I is henceforth fixed to 5.0×h, as this provides good accuracy for both regular and irregular domains.

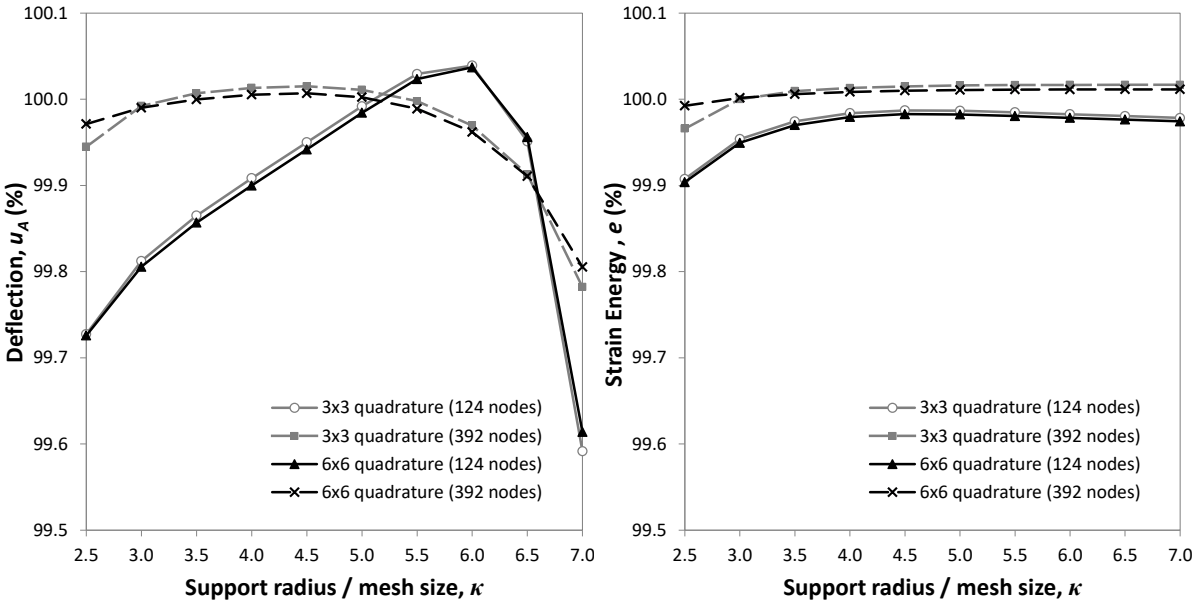

Figure 10 – Effect of support radius on (a) deflection of point A and (b) system strain energy

4.1.2. Domain integration

The multi-level rectangular grid (MLRG) approach developed for integration of irregular domains is investigated here. Consideration is given to the most computationally efficient way to integrate the domain function without compromising accuracy, possibly by optimising the number of quadrature points. Since the distribution of Gauss points is based on rectangular cells, the first important concern is to ensure that the coverage of cells over the domain is maximised. In the MLRG approach, this is mainly controlled by the level of rectangular grid. The second concern relates to the required number of quadrature points per integration cell. Note that the size of the cells reduces in the vicinity of the curved edges, as discussed earlier. Therefore, in order to avoid unnecessary computational effort in integrating small cells, a simplification is made here whereby the quadrature order per cell is reduced as the cell size decreases. To address these two concerns, a numerical

parametric investigation is conducted, enabling the most appropriate combination of the number of cells, quadrature order and the level of rectangular grid to be established.

Figure 11 demonstrates the integration result of the total strain energy for the current problem. The EFG discretisation is based on 20×25 grid with a total of 392 nodes. Two sets of background grid are chosen for integration cells, each of which employs different quadrature rules and rectangular grid levels. Except for the coarse 8×10 grid with 3×3 quadrature, it is clear from the figure that the effect of increasing the Gauss points appears to be insignificant. In fact, the use of more integration cells appears to be more important, as evident from comparing the results for the 8×10 and 16×20 grids. It is also noted that a high level of MLRG, between 6 and 8 levels, is required to establish accurate integration – higher than that, the return in accuracy for computational effort is significantly diminished. For consistency, a grid of 16×20 cells with 4×4 quadrature rules and 6 levels of MLRG is proposed as the optimal integration scheme for a unit cell panel. Comparing the proposed MLRG integration to the original single-level approach of Belytschko & Lu [25] in Figure 12, it is evident that the new MLRG approach offers a more consistent integration with a greater level of accuracy.

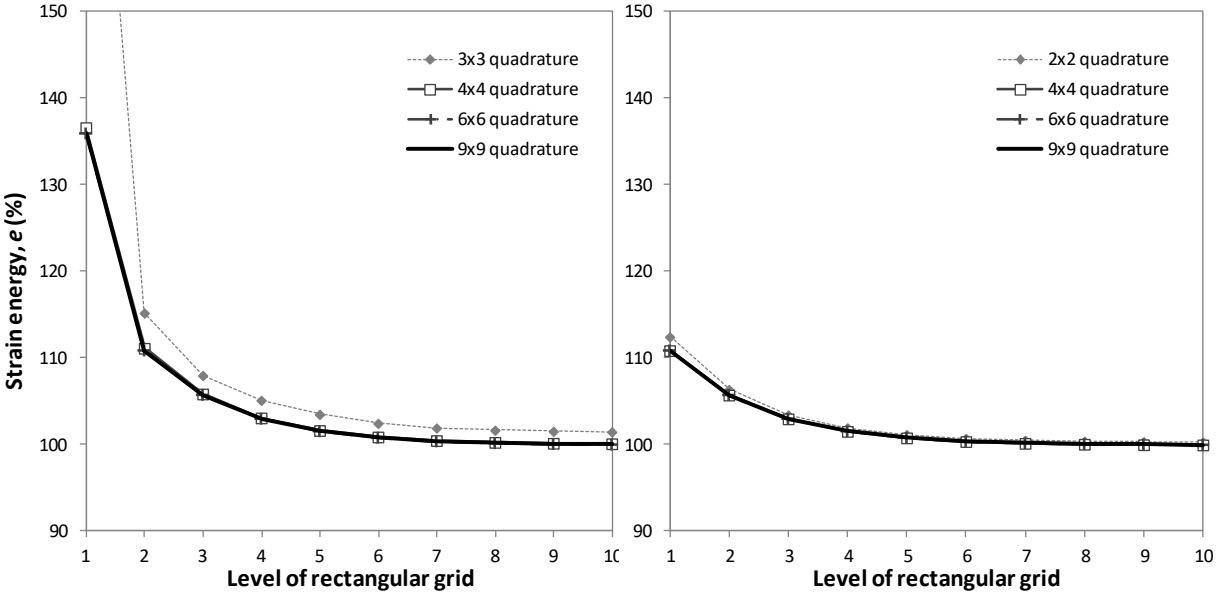

(a) Main grid of 8 x 10

(b) Main grid of 16 x 20

Figure 11 – Prediction of strain energy for different quadrature schemes

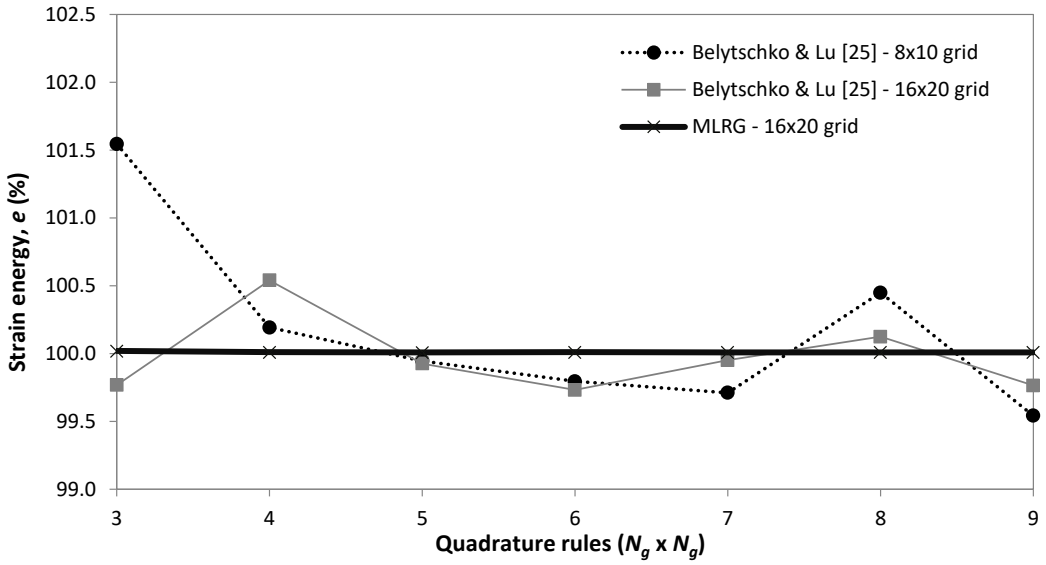

Figure 12 – Comparison between MLRG integration and approach of Belytschko & Lu [25]

4.1.3. Convergence of displacements

The vertical displacement at point A of the unit cell under transverse compression has been shown earlier in Figure 9(b), where good agreement of the nodal displacements is observed between the EFG and FEA models using a much smaller number of EFG nodes ($N_{EFG} \ll N_{FEA}$). Detailed comparison considering the different levels of discretisation is provided in Figure 13, where it is evident that the EFG model converges much faster than the FEA model utilising the conforming 9-noded shell elements of ADAPTIC [32, 33] with increasing levels of nodal discretisation. Note that although the converged value of the EFG model appears to be slightly lower than the estimated exact solution based on the convergence rate of the FEA solution with conforming shell elements, all EFG predictions offer excellent accuracy with an error of less than 0.1%, even for the coarsest discretisation level of 124 nodes.

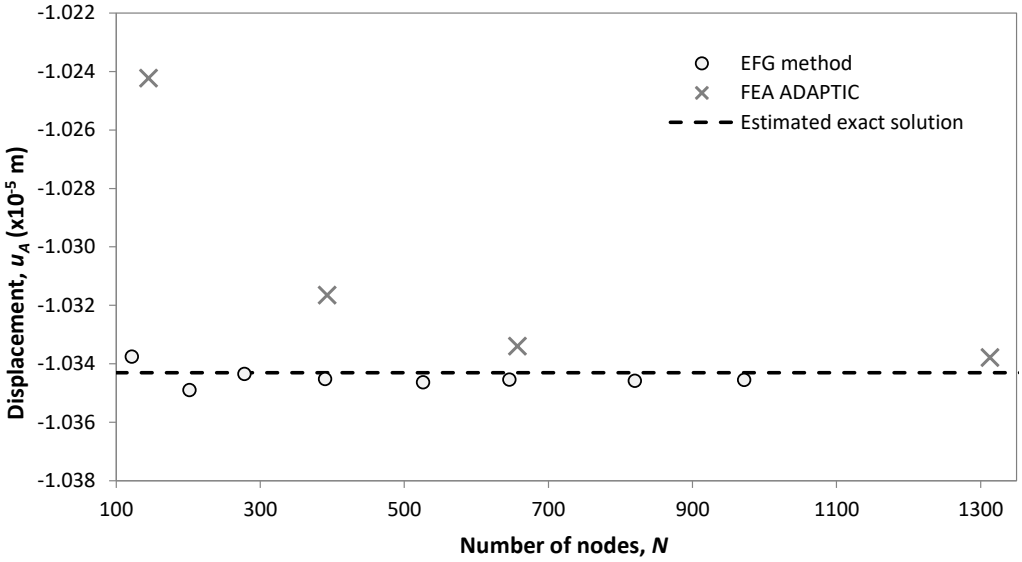

Figure 13 – Convergence of displacements for unit cell under compression

4.1.4. Convergence of energy

The distribution of the normal stresses σ_{xx} and σ_{yy} over the unit cell are shown in Figure 14 and Figure 15 respectively. Comparison of these stresses against FEA predictions is also made in detail, considering the stress along the panel depth at x = S/2 as illustrated in Figure 14(c) and Figure 15(c). It can be seen that the EFG model is capable of achieving high-accuracy even for a coarse distribution of nodes (e.g. 124 nodes based on 10×13 grid). More importantly, the stresses are continuous within the domain unlike the FEA model which would normally require post-processing (e.g. by taking averaged nodal stresses between elements) for obtaining a smooth stress distribution. Finally, the prediction of strain energy by the EFG and FEA models, considering different levels of discretisation, is presented in Figure 16. Clearly, the EFG model is superior to the FEA model, where excellent prediction of the strain energy can be achieved with as few as 124 nodes, whereas the FEA model employing the 9-noded quadratic shell elements requires more than 1300 nodes for comparable accuracy.

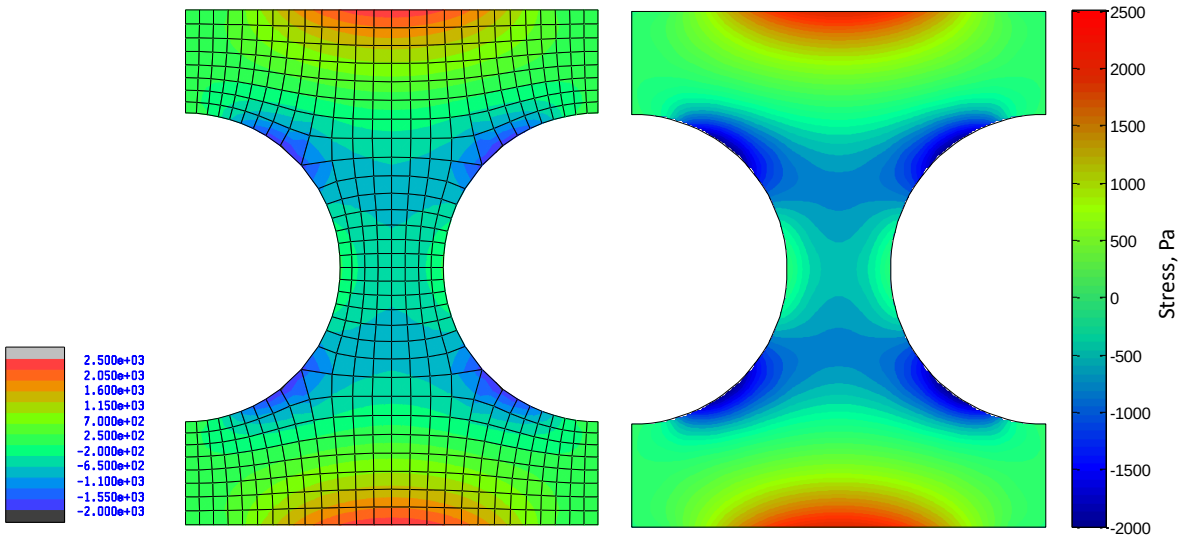

(a) FEA ADAPTIC (2261 nodes) (b) EFG method (392 nodes)

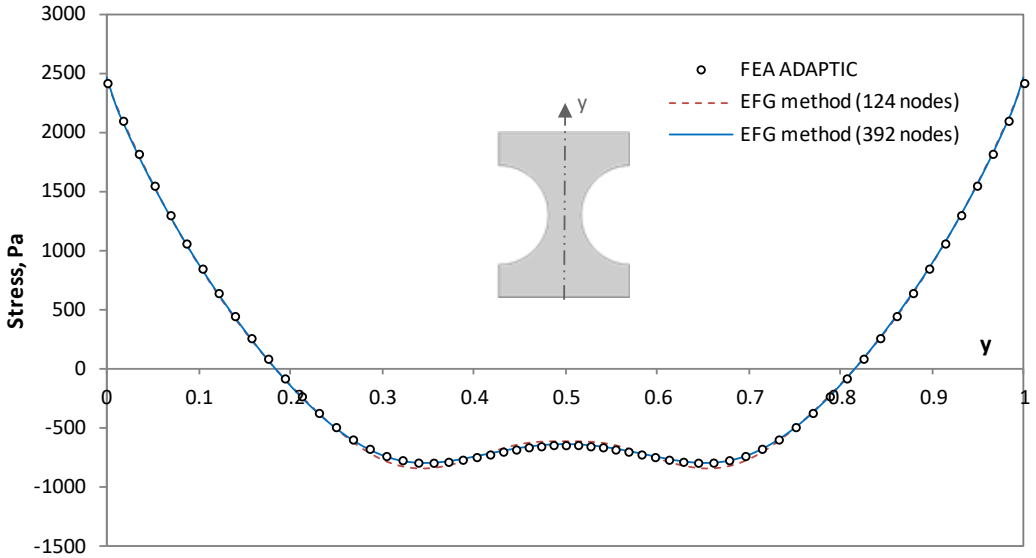

(c)

Figure 14 – Distribution of normal stress σ_{xx} (a)-(b) over unit cell and (c) over depth at x = S/2

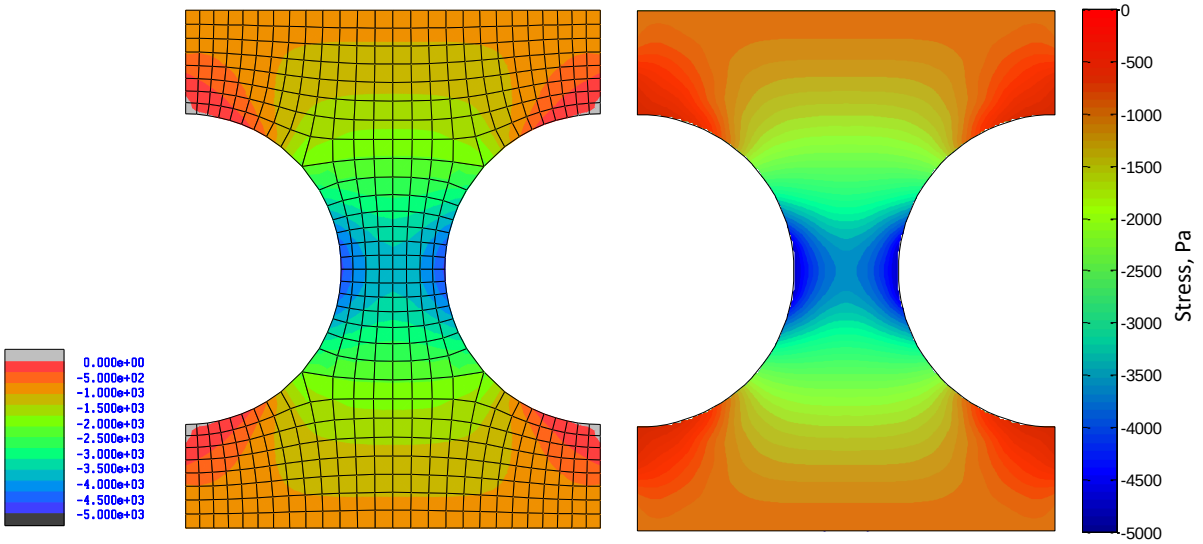

(a) FEA ADAPTIC (2261 nodes) (b) EFG method (392 nodes)

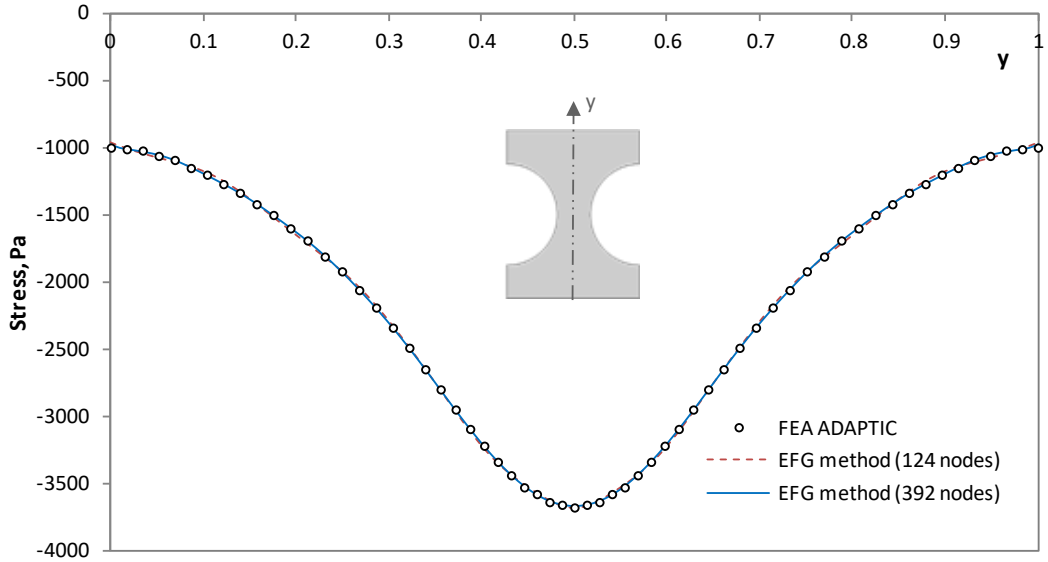

(c)

Figure 15 – Distribution of normal stress σ_{yy} (a)-(b) over unit cell and (c) over depth at x = S/2

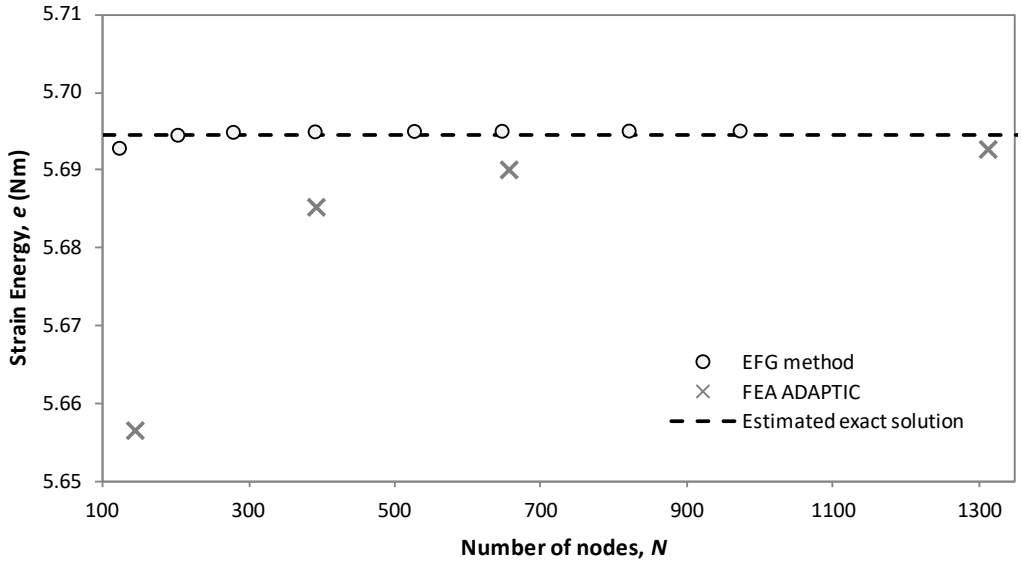

Figure 16 – Convergence of strain energy for unit cell under compression

4.2. Unit cell under shear

The same unit cell as in the previous example is now considered with different boundary conditions and loading, where, as shown in Figure 17(a), the panel is clamped along the left side edges and is horizontally restrained along the right side edges where shear tractions are applied. The two alternative levels of discretisation as in the preceding example, namely 124 nodes based on a 10×13 grid and 392 nodes based on a 25×16 grid, are also considered. The estimated exact solution, obtained from a detailed FEA model using ADAPTIC, is determined for the vertical displacement as $u_A = -1.7308\times10^{-5}$m and for the total strain energy as $e = 3.4904$ N.m.

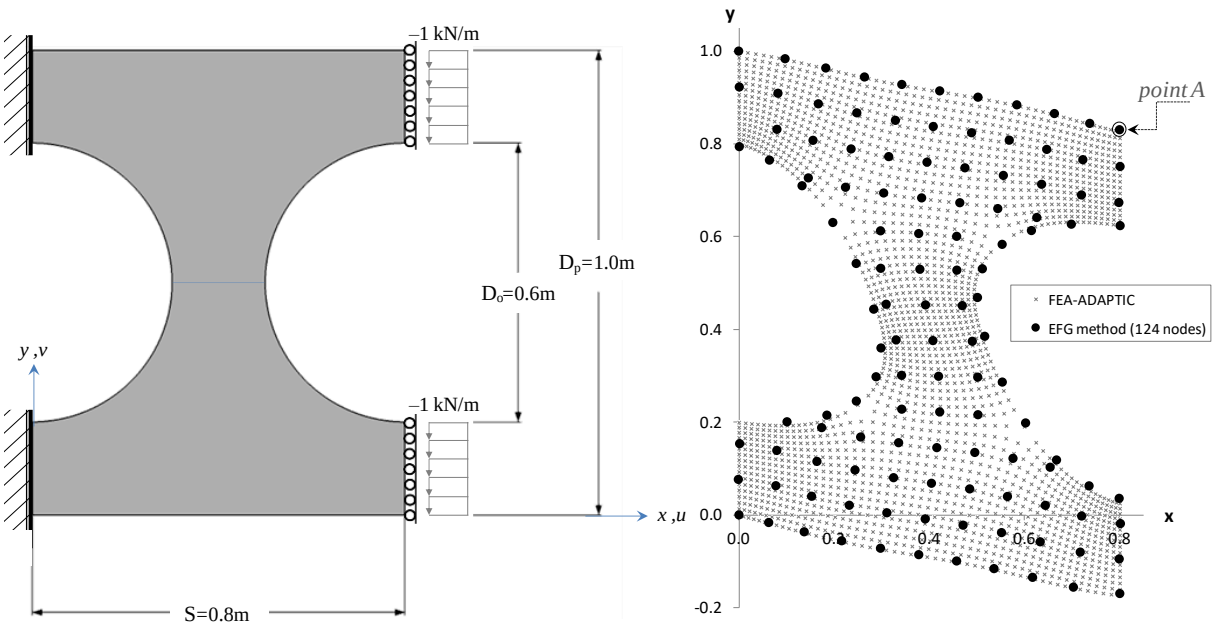

Figure 17 – Unit cell under shear: (a) applied loads and boundary conditions, (b) distribution of nodes and deflected shapes with EFG and FEA models

4.2.1. Domain integration

The prediction of strain energy is summarised in Figure 18 for cases with background cells of grid 8×10 and grid 16×20. The latter provides a better prediction of the exact solution especially for a low level of MLRG subdivision. However, employing at least 6 levels of rectangular grid for both sets is necessary to achieve good accuracy with an error less than 0.5%, which is consistent with the previous example of the unit cell under transverse compression.

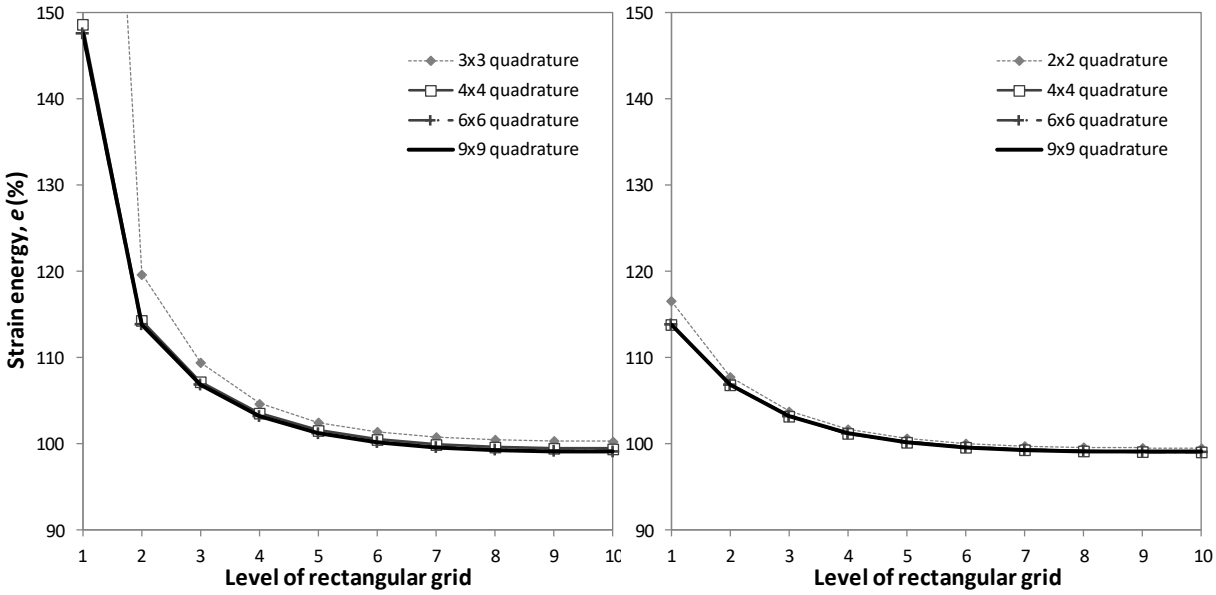

(a) Main grid of 8 x 10

(b) Main grid of 16 x 20

Figure 18 – Strain energy resulting from different quadrature schemes

4.2.2. Convergence of displacements

The deflected shape of the unit cell under the applied shear loading is depicted in Figure 17. The convergence of displacements for this problem is presented in Figure 19 for the EFG model compared with the FEA model utilising the 9-noded conforming shell element, specifically considering the displacement of point A. For the same number of nodes, the EFG model exhibits better accuracy than the FEA model, and it converges quickly to the exact solution when the total nodes approach 600 compared to over 1300 for the FEA model. Except for the coarsest discretisation of 124 nodes, all subsequent EFG models provide an accuracy for u_A within 0.1%.

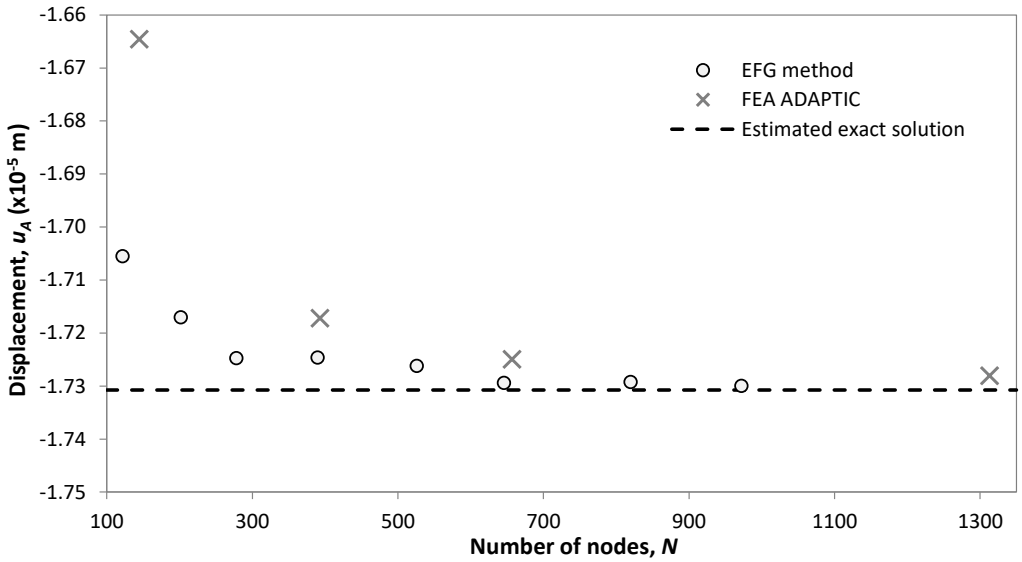

Figure 19 – Convergence of displacements for unit cell under shear

4.2.3. Convergence of energy

The distribution of shear stresses τ_{xy} in the unit cell is depicted in Figure 20, where good agreement is observed between the EFG and FEA results. For a detailed quantitative comparison, the distribution of τ_{xy} across the depth of the panel (at x = S/2) is presented in Figure 20(c), where the prediction of the EFG model with 124 nodes shows slight discrepancies near the two ends and at mid-depth, though these discrepancies are considerably reduced with the finer model using 392 nodes. Finally, Figure 21 depicts the prediction of strain energy using the EFG and FEA models, where it is again evident that the EFG models offer a better convergence rate compared to the FEA models.

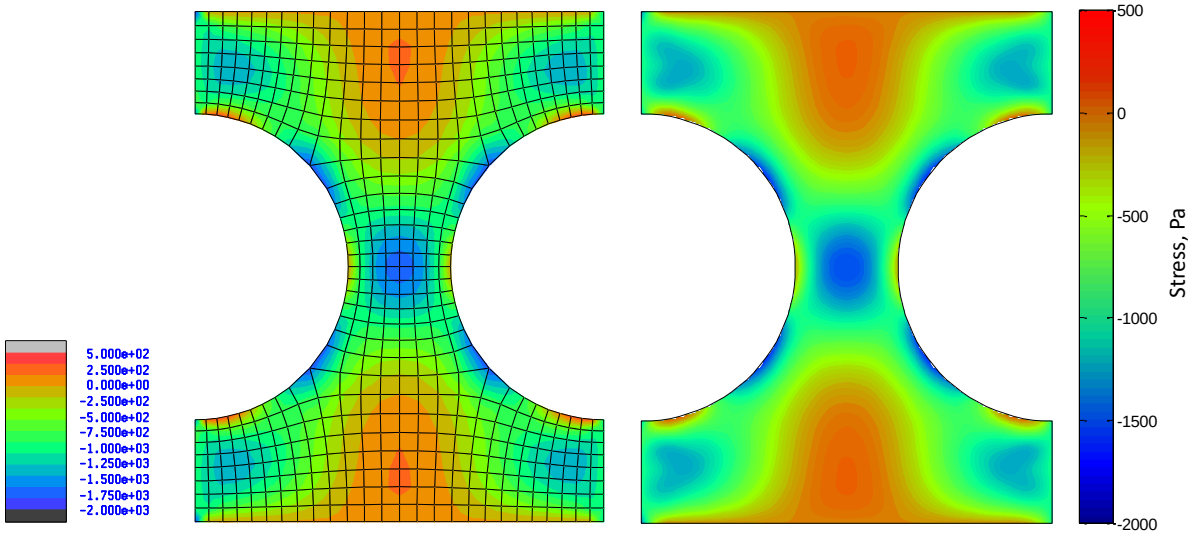

(a) FEA ADAPTIC (2261 nodes) (b) EFG method (392 nodes)

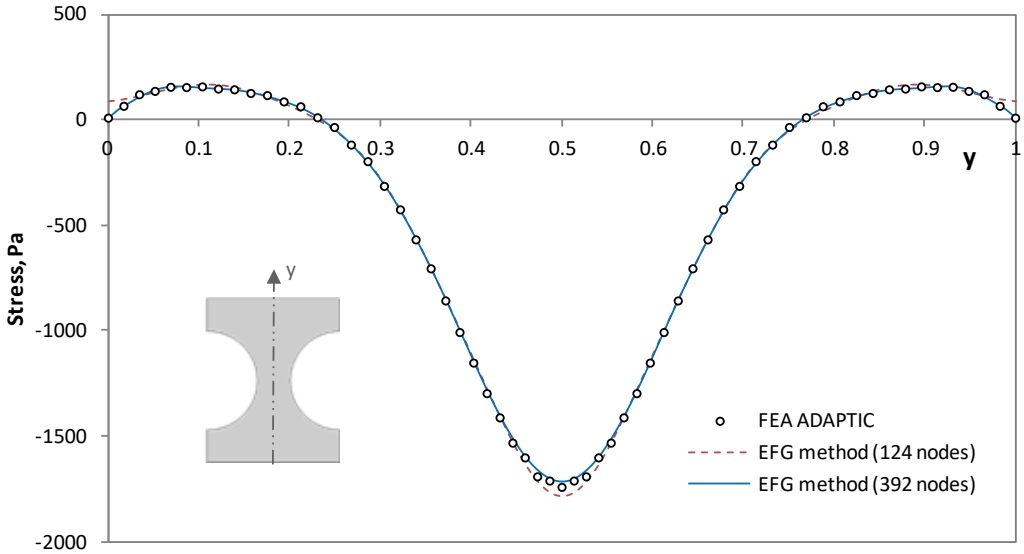

(c)

Figure 20 – Distribution of shear stress τ_{xy}(a)-(b) over unit cell and (c) over depth at x = S/2

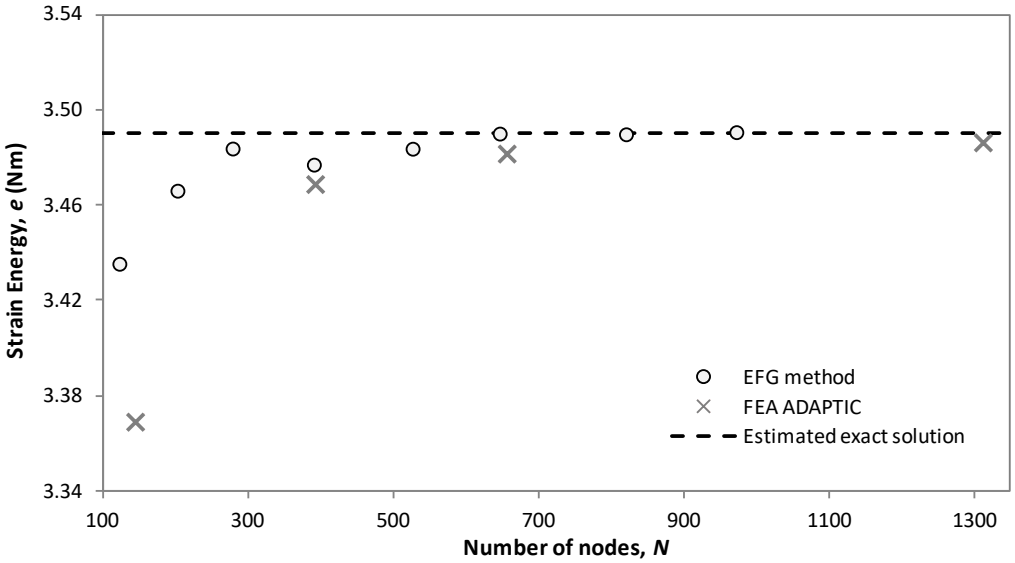

Figure 21 – Convergence of strain energy for unit cell under shear

5. Application to Cellular Beams

Several examples of cellular beam problems are presented here to demonstrate the performance of the proposed unit-based EFG method. In particular, the ability of this method to obtain accurate predictions of the planar response is highlighted in comparison with 2D FEA models using ADAPTIC in terms of the number of nodes. In all cases, the support radius r_I is taken as 5×h, while the weight function parameters are taken as k = 1 and c = r_I/ 4. The previously established quadrature rule of 4×4 per cell with 6 levels of MLRG is employed for domain integration. Again, the 'exact' solution for these problems is estimated from a detailed FEA model utilising a very fine mesh.

5.1. Simply supported cellular beam under UDL

A relatively short cellular beam of length L = 7.92m and overall depth D_p = 1.603m, hole diameter D_o = 0.8m and spacing S = 1.472m is considered. The beam is simply-supported and produced from an original I-section of UB1016×305×222 with web thickness t_w = 16mm, flange thickness t_f = 21.1mm and flange width b_f = 300mm. Five holes are symmetrically introduced along the length and 1.0 kN/m UDL is applied on top of the beam, as shown in Figure 22. The material properties are taken asYoung's modulus E= 210×10^9N/m^2 and Possion's ratio υ = 0.3.

Figure 22 demonstrates the deflected shape of the simply-supported beam under UDL, comparing the results between detailed FEA and the proposed EFG approach. Point A in the figure depicts the location with the maximum vertical displacement, which is being used as a reference point for detailed comparison, where the results are shown in Figure 23. Although the EFG method is considered with the unit-cell approach, the total number of nodes N over the whole beam is used for comparing the relative accuracy of FEA and EFG predictions. The estimated exact solution $u_{A(exact)}$ is -2.9279×10^{-5}m, and the FEA-ADAPTIC using the 9-noded conforming shell elements appears to predict the value reasonably well. On the other hand, the EFG method through the use of a unit-cell model provides a slightly more flexible result which is 1.5% lower than $u_{A(exact)}$. This relatively small disagreement is attributed to the unit-based approach used for establishing the overall cellular beam response. Since a flexibility-based super-element is adopted, where the displacements at the super-element nodes are averaged approximations from boundary displacements, there would be small displacement discrepancies, so-called compatibility defaults, between adjacent unit cells, which lead to the EFG unit-based solution being slightly more flexible.

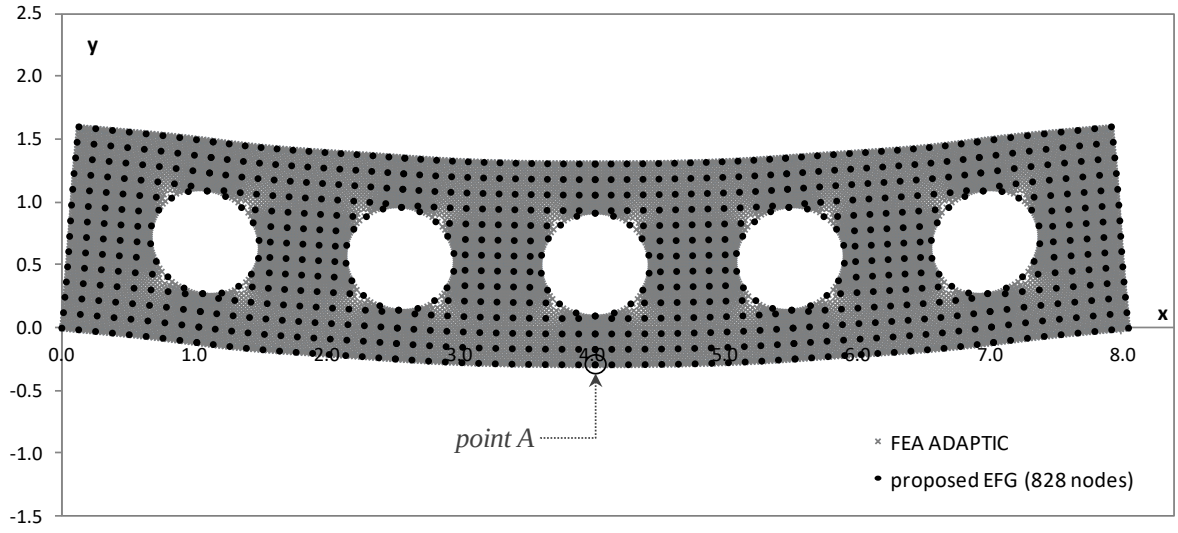

Figure 22 – Simply supported cellular beam under uniform distributed loading

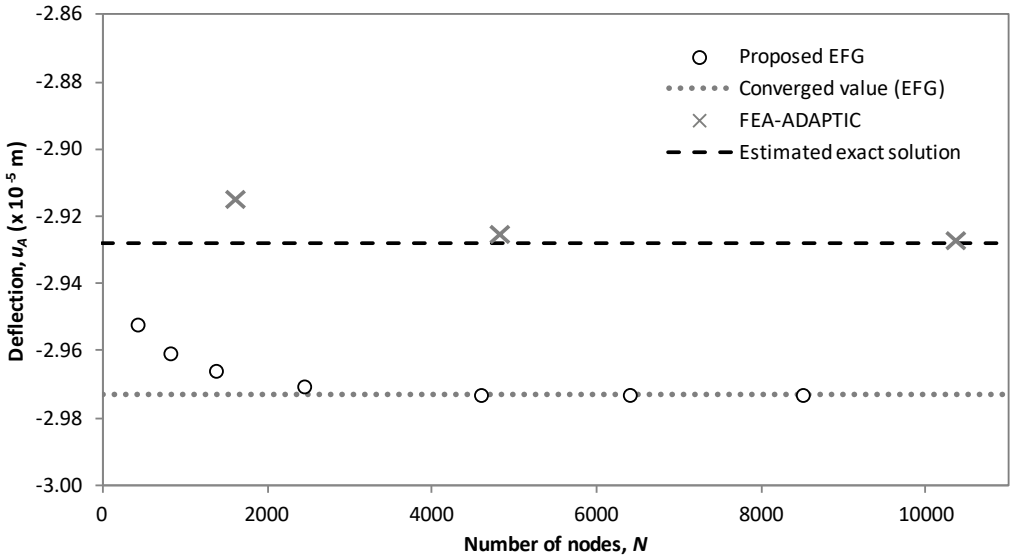

Figure 23 – Convergence of the deflection at point A for the simply supported beam

As illustrated in Figure 24, a favourable comparison against the detailed FEA model is achieved by the proposed EFG approach, despite the use of a modular formulation for the local unit-cell response. It can be seen that the EFG stress functions are readily continuous over the unit cells, whereas some post-processing would be required in FEA for smoothing the stresses value over the domain. Note that additional stress concentration near the beam supports in the EFG model is caused by the vertical restraints that are applied at the location of super-element nodes, while these restraints are distributed along the edges in the FEA model.

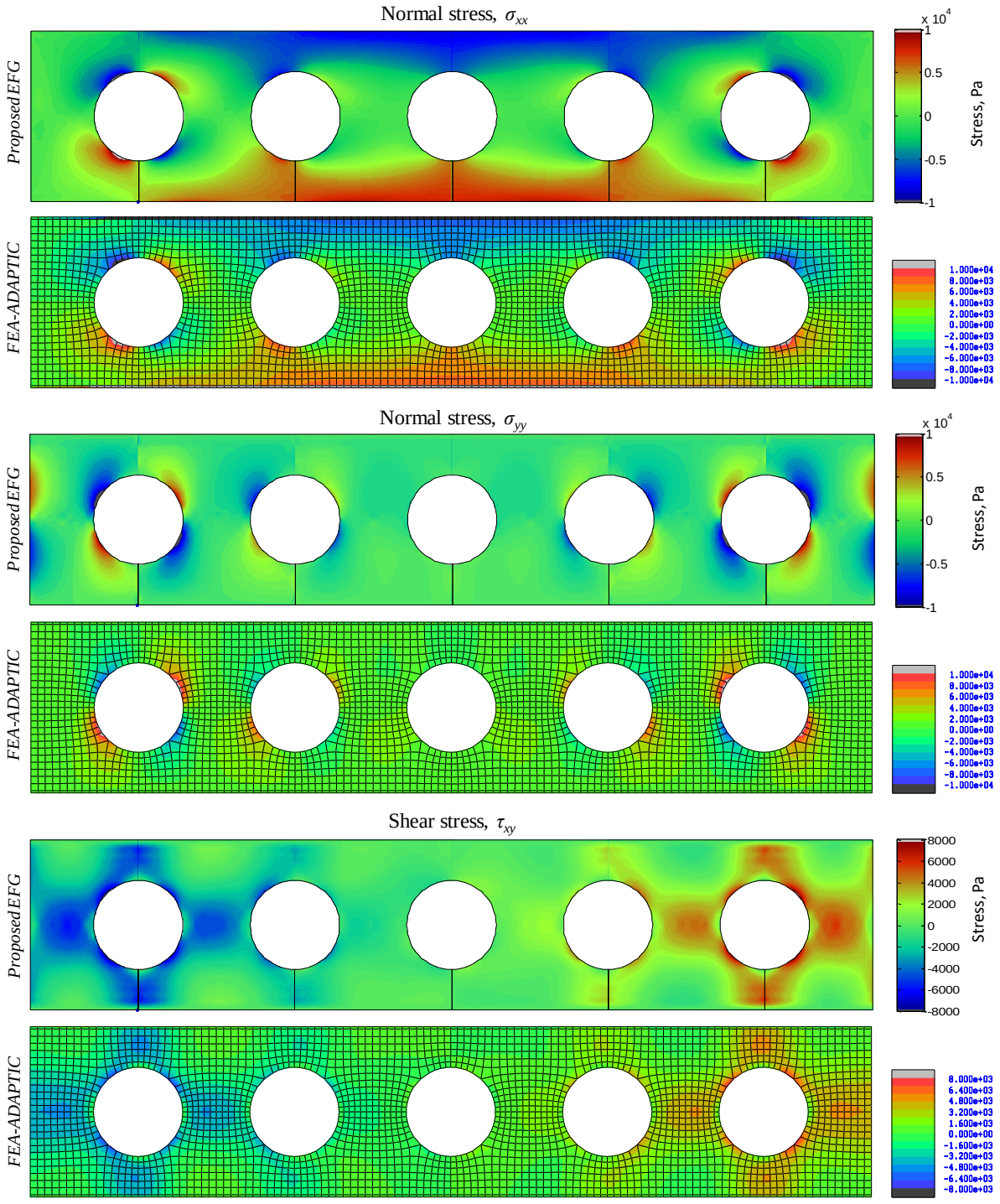

Figure 24 – Comparison of stress patterns between the proposed EFG and detailed FEA

The strain energy predicted by the proposed EFG approach is depicted in Figure 25, where the prediction is slightly higher than that of detailed FEA owing to the more flexible response by the EFG unit-based solution as discussed earlier. By considering only the result of the EFG analysis, favourable predictions with less than 0.1% error compared to the converged value are achieved when the total

number of nodes exceeds 2500, which is basically equivalent to an average 300 nodes per unit cell. This performance is consistent with the previously obtained result for a unit-cell analysis.

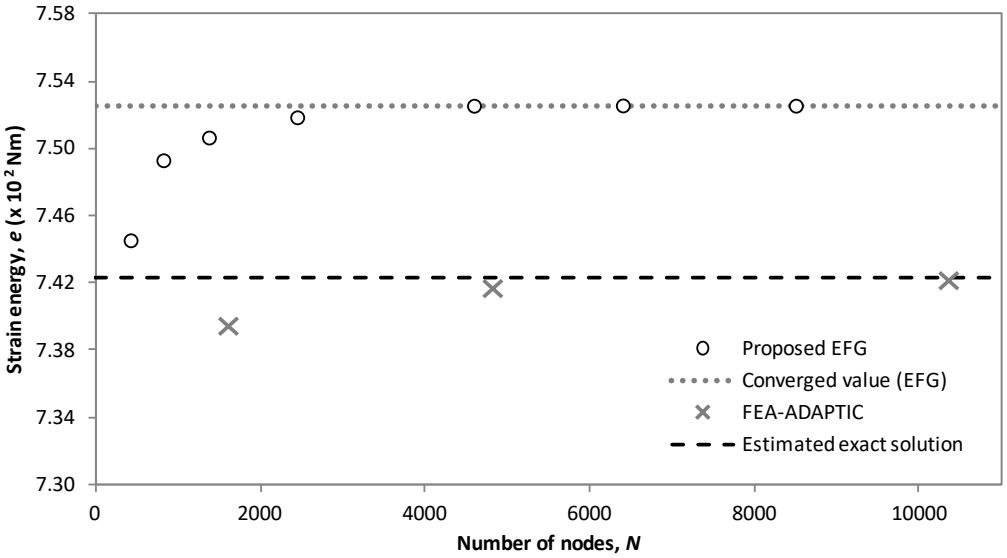

Figure 25 – Convergence of strain energy predictions for simply-supported cellular beam

Finally, the convergence rate of the FEM and EFG solutions is investigated by considering the relative error (*re*) in the energy norm, which is related to the error in the predicted strain energy:

$$re = \frac{\left| e_{conv} - e_{pred} \right|}{\left| e_{conv} \right|} \tag{42}$$

where e_{pred} is the predicted strain energy and e_{conv} is the converged/estimated exact solution. A comparison between the FEM and EFG convergence performance is depicted Figure 26 in terms of a non-dimensional characteristic mesh size h_e, which for a 2D problem is related to the number of nodes (N) by:

$$h_e = 1 \Big/ \sqrt{N} \tag{43}$$

It can be observed that the FEM solution achieves the optimal convergence rate expected from a quadratic element with $re = \mathbf{O}\left(h_e^4\right)$. On the other hand, the proposed EFG unit-cell method attains a similar convergence rate for a coarse level of discretisation, though it notably achieves an improved and accelerated rate as the level of discretisation becomes finer.

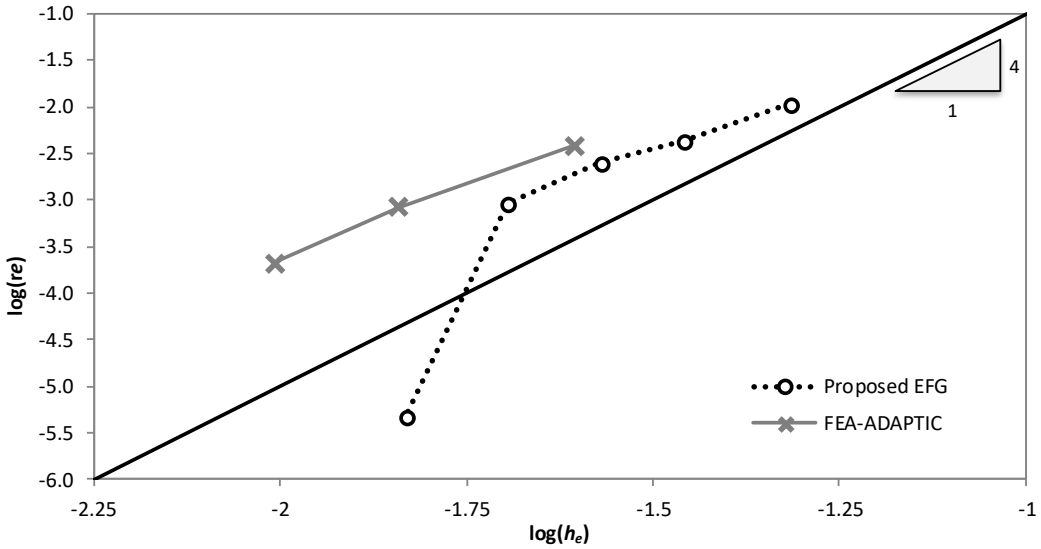

Figure 26 – Convergence rates of EFG and FEM predictions for simply-supported cellular beam

5.2. Cellular beams with different support conditions

Further verification for cellular beams with different support conditions is presented here. Two particular cases are chosen: 1) both beam ends are fully fixed, and 2) only one end is fixed with the other end free thus corresponding to a cantilever condition. An identical beam geometry to the previous example is used, and a UDL of 1.0 kN/m is applied to top of the beam.

5.2.1. Fully clamped cellular beam

Since the developed model is based on 4-noded super-elements, the enforcement of the fixed end supports can only be made based on associated freedoms of super-element nodes, though this should not cause significant discrepancy. The deformed shape of the fully clamped beam under UDL is depicted in Figure 27, while the result comparisons based on point A are provided in Figure 28. Again, the simplified EFG approach slightly overestimates the detailed FEA solution $(u_{A(exact)} = -1.3984\times10^{-5} m)$ due to possible discrepancy between the connecting super-elements and also at the fixed supports. The same applies to the estimation of the corresponding strain energy shown in Figure 29, where a slight overestimate standing at less than 1.5% is observed. Considering the EFG solutions, an error within 0.1% of the converged solution is achieved when the total number of nodes reaches approximately 3000 nodes, compared to more than 10000 nodes with FEM. Finally, in terms

of the convergence rate, the proposed EFG unit-cell method exhibits again a better performance compared to FEM, with an accelerated rate as the level of discretisation becomes finer, as depicted in Figure 30.

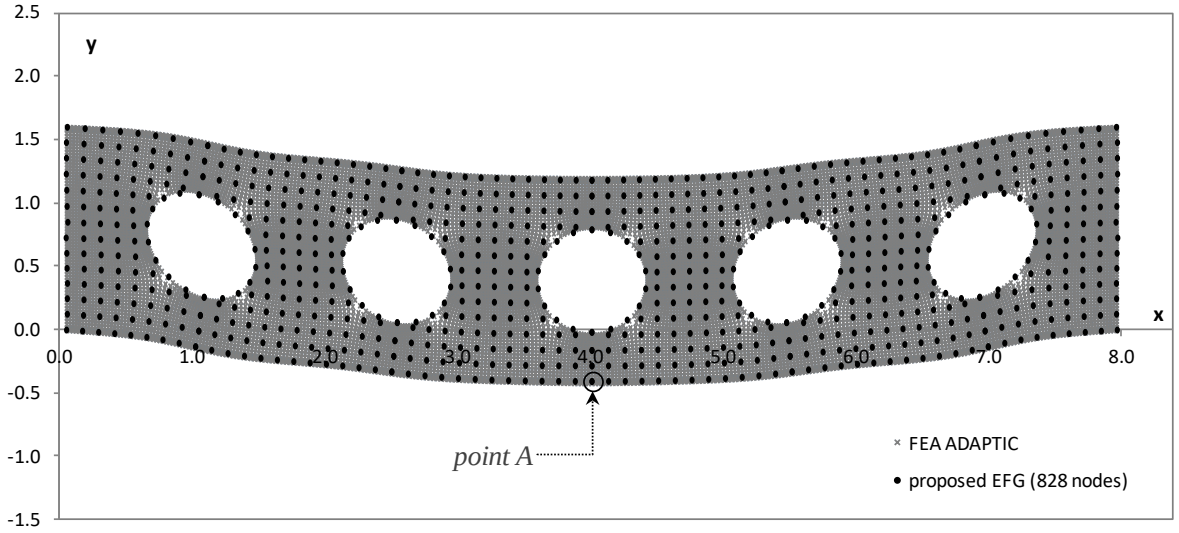

Figure 27 – Fully clamped cellular beam under uniform distributed loading

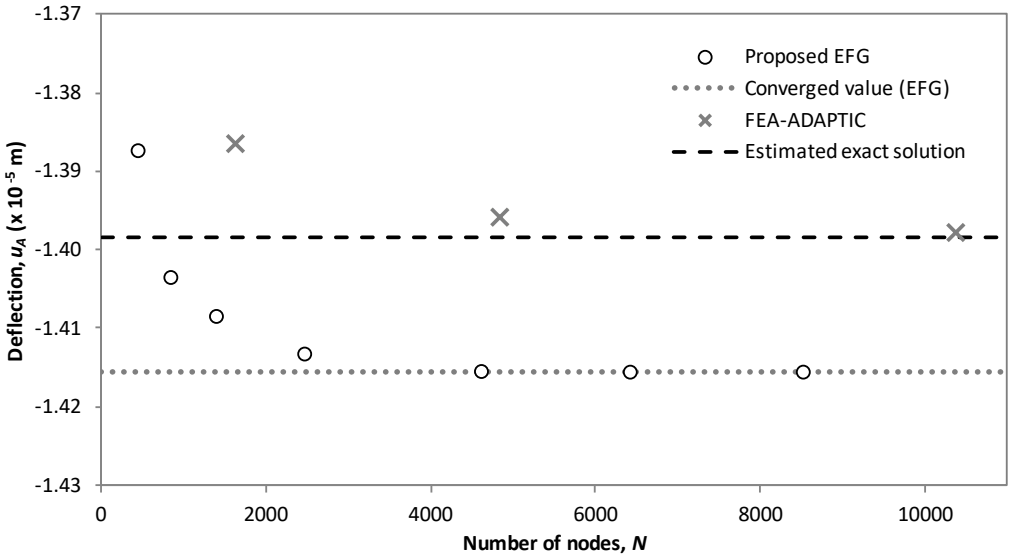

Figure 28 – Convergence of the deflection at point A for the fully clamped cellular beam

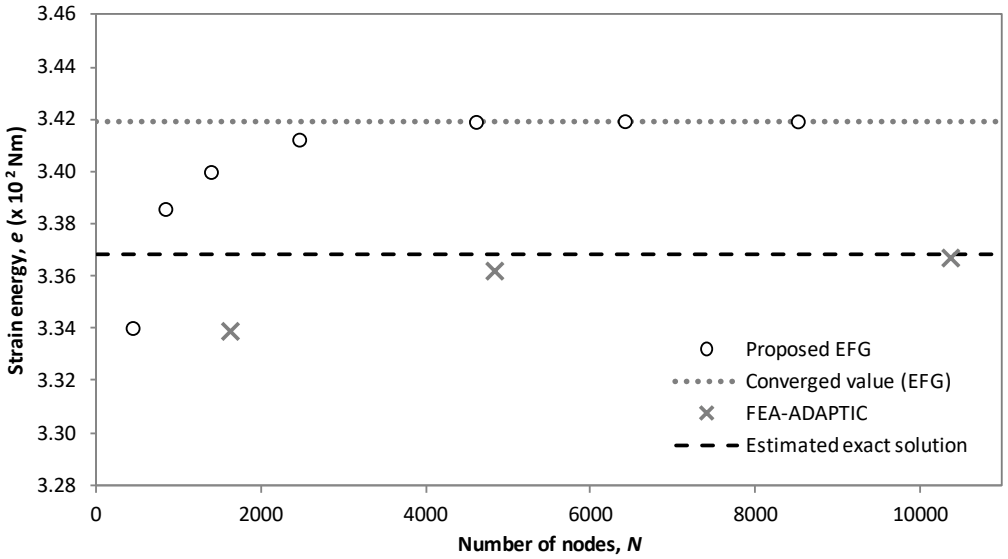

Figure 29 – Convergence of the strain energy for the fully clamped cellular beam

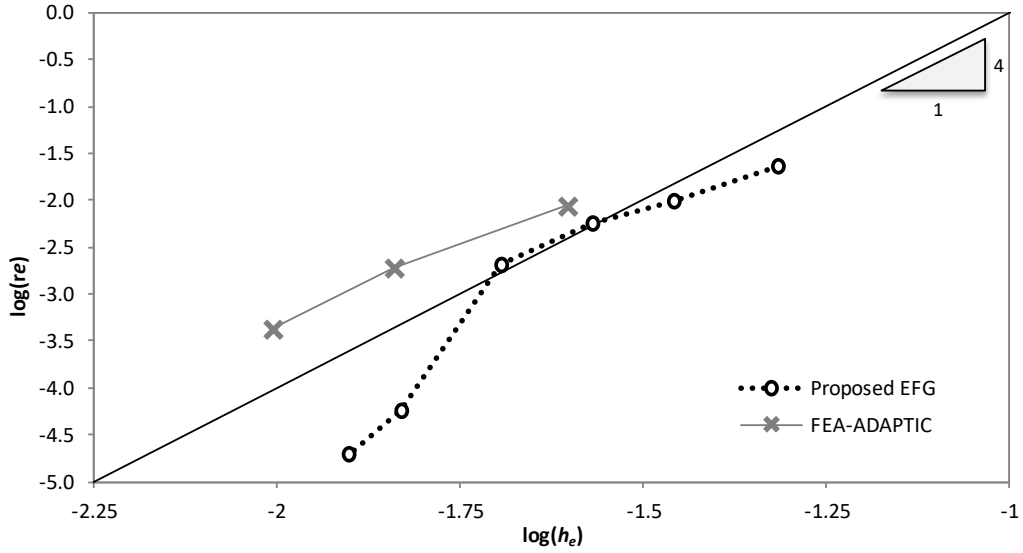

Figure 30 – Convergence rate of EFG and FEM predictions for fully clamped cellular beam

5.2.2. Cantilever cellular beam

The same beam subjected to UDL along the top edge is now considered under cantilever conditions. As depicted in Figure 31, the proposed EFG approach provides favourable comparison against detailed FEA in relation to the deformed shape. In terms of the prediction of the maximum deflection at point A, the EFG approximation shows a promising result with 0.2% compared to the estimated exact solution ($u_{A(exact)}$ = –2.3142×10^{-5}m) as presented in Figure 32. The corresponding

strain energy prediction is also within 0.35% of the estimated exact solution (Figure 33). Furthermore, considering the convergence of both methods shown in Figure 34, a better convergence rate is achieved by the proposed method similar to the two previous cases. Nevertheless, it is noted that, the performance of the EFG method for the cantilever beam is marginally better than the two previous cases, which suggests that the compatibility defaults for the cantilever condition are reduced in comparison with the simply supported and fully clamped conditions.

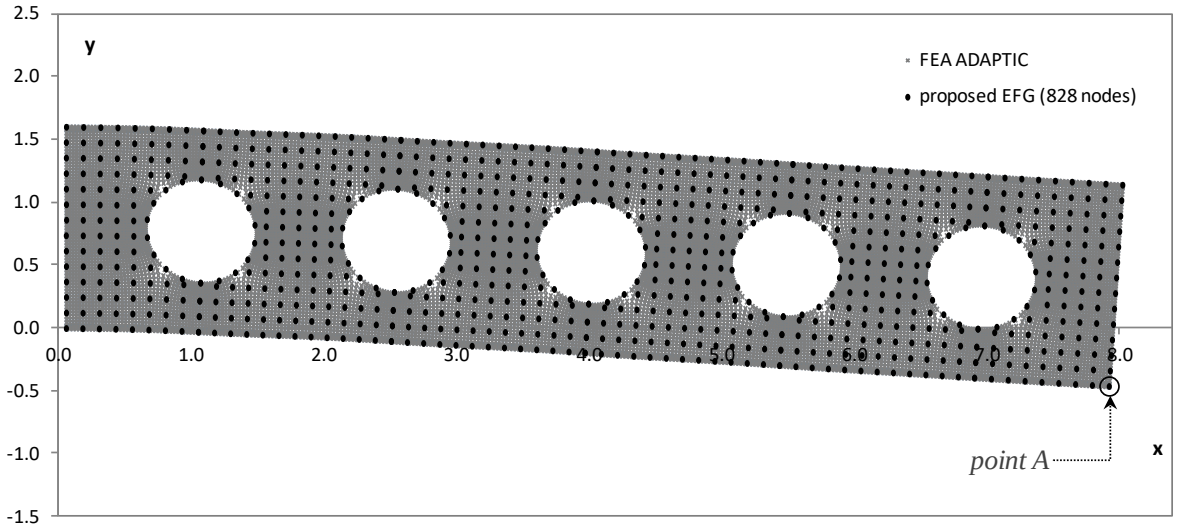

Figure 31 – Cantilever cellular beam subjected to uniformly distributed loading

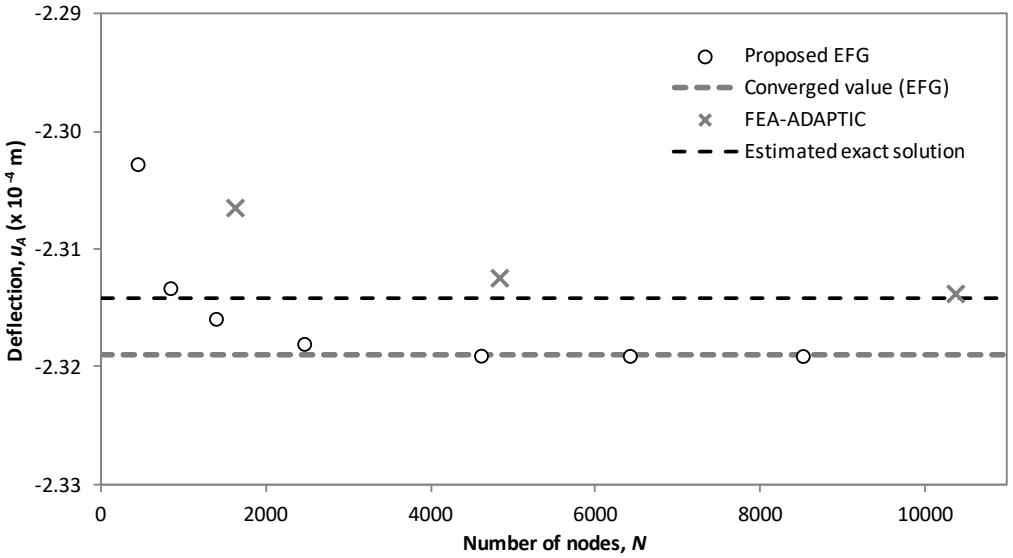

Figure 32 – Convergence of the deflection at point A for the cantilever cellular beam

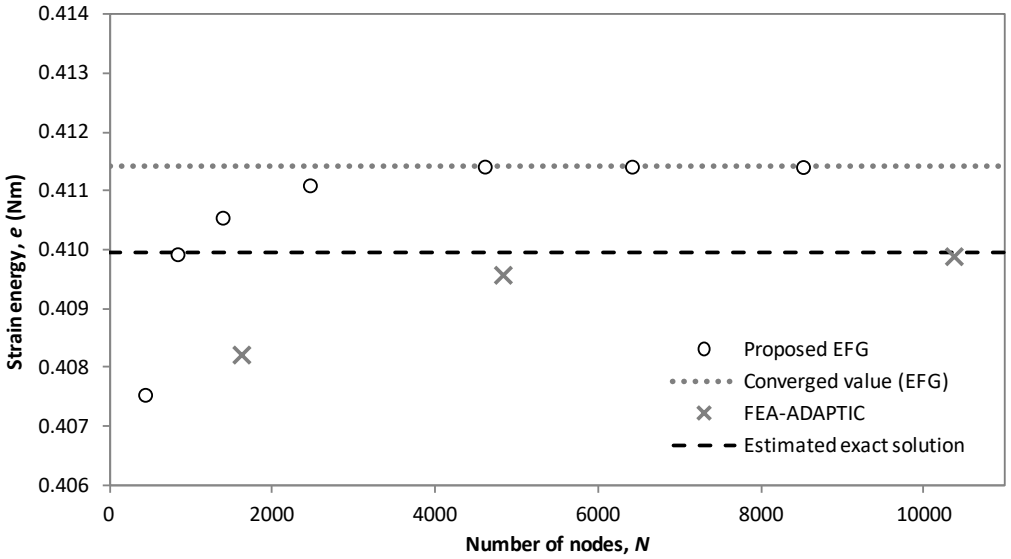

Figure 33 – Convergence of the strain energy for the cantilever beam

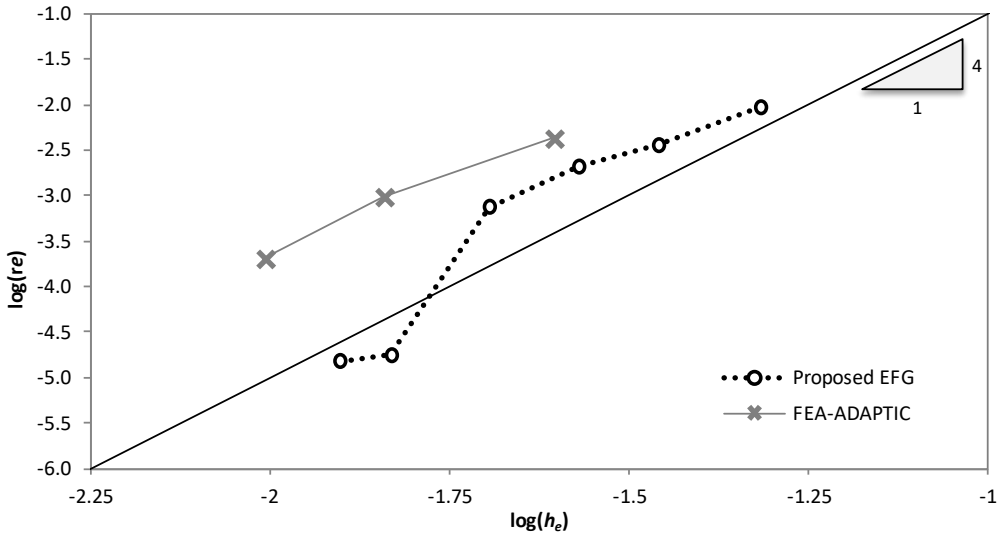

Figure 34 – Convergence rate of EFG and FEM predictions for cantilever cellular beam

5.3. Computational benefits of EFG method for increasing number of holes

The proposed EFG approach benefits from the repetitiveness of cells in typical cellular beam profiles, whereas conventional FEA suffers from the need to use more elements and nodes for accurate prediction in proportion to the number of holes. To highlight these benefits, simply supported cellular beams with an increasing number of web openings, varying from 2 to 21 holes, are analysed, and the results are summarised in Figure 35. With an excellent comparison between the EFG and FEA results in relation to the predicted strain energy, the proposed EFG method consumes a remarkably small

computing time regardless of the number of holes compared to the FEA models, where the reported computing times include all element/unit-cell computations, solution of equations and stress recovery. The superior performance of the proposed EFG unit-cell approach is mainly due to the focus of the computation on the three unit-cells (left, right and internal cells), where the internal unit-cells are duplicates of the same internal super-element. It should be noted though that the comparison of computing time is only indicative, since the proposed EFG approach is implemented using MATLAB, while the FEA model employs ADAPTIC which is implemented using the FORTRAN programming language. An attempt to compare the results, particularly the computational time, between the proposed EFG method and a full scale model utilising only the EFG method (without the unit-cell formulation) also exhibited a far better performance by the novel unit cell idea than the conventional discretisation approach.

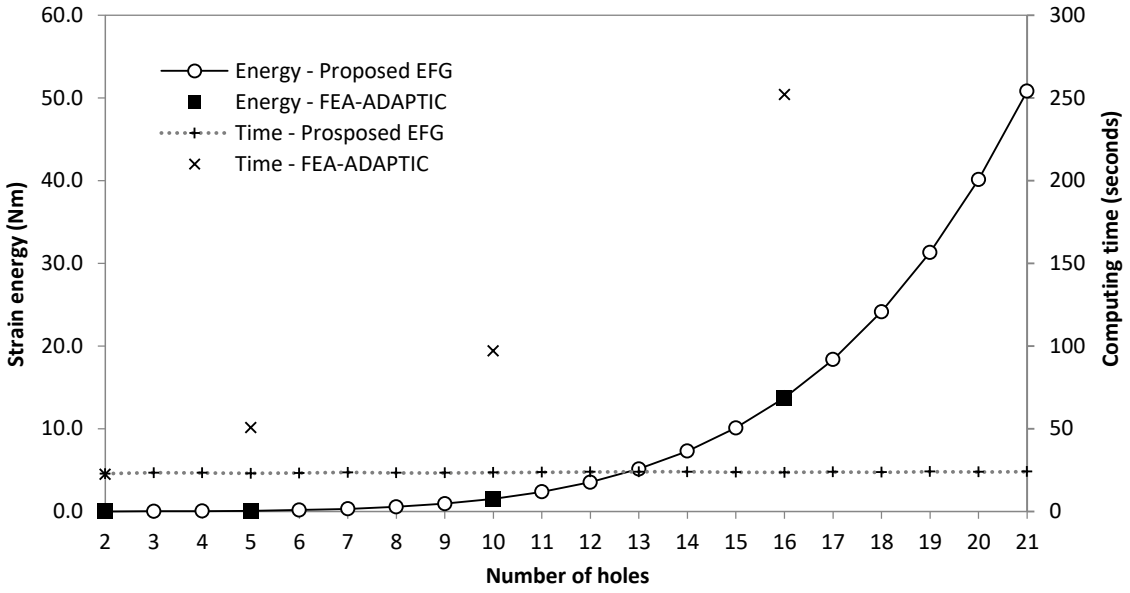

Figure 35 – Strain energy and computing time for cellular beams with varying number of holes

6. Conclusion

This paper presents an effective approach for modelling the planar response of cellular beams, in which the concept of a unit-cell super-element is introduced, which benefits further from the adoption and enhancement of the Element-Free Galerkin (EFG) method for establishing the super-element response characteristics. The main motivation of this work is the accurate and efficient determination of the planar stress distribution under in-plane loads, which is required for assessing local out-of-plane buckling in the web components of a cellular beam.

The EFG method offers significant advantages through its smooth and continuous shape functions, governed by a proper choice of the polynomial basis and weight functions, thus avoiding the need for post-processing of discontinuous stress predictions that are typical in finite element (FE) analysis. The essential boundary conditions are imposed via a penalty method, in which a careful selection of penalty factor is crucial to avoid numerical errors. An enhanced method of numerical integration is proposed in this work to deal with irregular domains, particularly in the vicinity of curved boundaries, where a multi-level rectangular grid (MLRG) approach is shown to provide optimal efficiency and accuracy in the solution. The numerical examples demonstrate that the present EFG model offers significantly better results with a smaller number of DOFs compared to FE models. In this respect, the use of nodes along curved boundaries, in addition to a simple arrangement of nodes based on a regular rectangular grid, is found essential to improve the accuracy of EFG predictions.

Besides the specific enhancements of the EFG approach for irregular domains, more significant computational benefits arise from the proposed concept of a ‘unit-cell’ formulation, which takes advantage of the repetitive profile in cellular beams with regular web holes. In this approach, the individual cell response is captured with a super-element utilising only four nodes, with a reduced number of DOFs and a corresponding set of representative actions, the characteristic response of which needs only to be determined once for a set of identical cells. Application examples considering cellular beams under different boundary conditions illustrate that deflection, stress pattern and strain energy predictions compare favourably against FE analysis, offering further an improved representation of the continuous stress field without the need for post-processing. Finally, the computational advantage of the proposed method are highlighted considering cellular beams with an increasing number of holes, where a drastically reduced computing time, proportional to the number of holes, is achieved compared to FE analysis.

The computational and modelling benefits of the proposed approach in predicting the planar response of cellular beams, paves the way for effective local buckling analysis of web components in such systems, as demonstrated in previous work of the authors [21] in the context of beams with arbitrary and irregular web openings. The extension of this local buckling approach to cellular beams with regular openings will be the subject of future work building on the current developments, thus offering a real prospect for accurate local buckling assessment of cellular beams within a computationally efficient framework, as necessary for practical application in design practice.

7. Acknowledgement

The funding provided by Universiti Teknologi Malaysia (UTM) for the PhD work of the first author at Imperial College London is gratefully acknowledged.

8. References

[1] British Steel Sections Plate and Commercial Steels. Design in Steel 4: Castellated and Cellular Beams, 1995.

[2] ArcelorMittal. Long Carbon Europe Sections and Merchant Bars: ACB Cellular Beams, 2008.

[3] New Steel Construction. In the grove. NSC Annual Review Januari 2016: The British Constructional Steelwork Association Ltd; 2016. p. 16.

[4] Sonck D, Van Impe R, Belis J. Experimental investigation of residual stresses in steel cellular and castellated members. Construction and Building Materials 2014;54:512-9.

[5] Srimani SL, Das PK. Finite Element Analysis of Castellated Beams. Computers and Structures 1978;9:169-74.

[6] Hoffman RM, Dinehart DW, Gross SP, Yost JR. Analysis of Stress Distribution and Failure Behavior of Cellular Beams. Proceedings of the 2006 ANSYS Conference; 2006; Pittsburgh, P A.

[7] Aglan AA, Redwood RG. Web Buckling in Castellated Beams. Proceedings of the Institution of Civil Engineers Part 2-Research and Theory 1974;57:307-20.

[8] Kerdal D, Nethercot DA. Failure modes for castellated beams. Journal of Constructional Steel Research 1984;4:295-315.

[9] Okubo T, Nethercot DA. Web post strength in castellated steel beams. Proceedings of the Institution of Civil Engineers, Part 2; 1985.

[10] Institution BS. Structural use of steelwork in building. Part 1: Code of practice for design - Rolled and welded sections. London, U.K.: British Standard Institution; 2000.

[11] Institution BS. Eurocode 3: Design of steel structures. Part 1-1: General rules and rules for buildings. London, U.K.: British Standard Institution; 2005.

[12] Westok. The Westok Cellular Beam. http://www.kloecknermetalsuk.com/kloecknerwestok/software-download/, 2016 (accessed 01.04.16).

[13] Lawson RM. Design for Openings in the Webs of Composite Beams: CIRIA Special Publication 51 / SCI Publication 068, 1987.

[14] Ward JK. Design of composite and non-composite cellular beams: SCI Publication 100, 1990.

[15] Zaarour W, Redwood R. Web buckling in thin webbed castellated beams. Journal of Structural Engineering-Asce 1996;122:860-6.

[16] Redwood R, Demirdjian S. Castellated beam web buckling in shear. Journal of Structural Engineering-Asce 1998;124:1202-7.

[17] Redwood RG. Behaviour of composite castellated beams: 2000.

[18] Lawson RM, Lim J, Hicks SJ, Simms WI. Design of composite asymmetric cellular beams and beams with large web openings. Journal of Constructional Steel Research 2006;62:614-29.

[19] Wong VB, Burgess I, Plank R. Behaviour of Composite Cellular Steel - Concrete Beams at Elevated Temperatures. International Journal of Steel Structures 2009;9:29-37.

[20] Panedpojaman P, Thepchatri T, Limkatanyu S. Novel design equations for shear strength of local web-post buckling in cellular beams. Thin-Walled Structures 2014;76:92-104.

[21] Zainal Abidin AR, Izzuddin BA. Meshless local buckling analysis of steel beams with irregular web openings. Engineering Structures 2013;50:197-206.

[22] Belytschko T, Krongauz Y, Organ D, Fleming M, Krysl P. Meshless methods: An overview and recent developments. Computer Methods in Applied Mechanics and Engineering 1996;139:3-47.

[23] Atluri SN, Zhu TL. New concepts in meshless methods. International Journal for Numerical Methods in Engineering 2000;47:537-56.

[24] Liu GR. Meshfree Methods: Moving Beyond the Finite Element. 2nd ed: CRC Press; 2010.

[25] Belytschko T, Lu YY, Gu L. Element-Free Galerkin Methods. International Journal for Numerical Methods in Engineering 1994;37:229-56.

[26] Atluri SN, Zhu TL. The meshless local Petrov-Galerkin (MLPG) approach for solving problems in elasto-statics. Computational Mechanics 2000;25:169-79.

[27] Nayroles B, Touzot G, Villon P. Generalizing the finite element method: Diffuse approximation and diffuse elements. Computational Mechanics 1992;10:307-18.

[28] Nguyen VP, Rabczuk T, Bordas S, Duflot M. Meshless methods: A review and computer implementation aspects. Mathematics and Computers in Simulation 2008;79:763-813.

[29] Rabczuk T, Belytschko T. Adaptivity for structured meshfree particle methods in 2D and 3D. International Journal for Numerical Methods in Engineering 2005;63:1559-82.

[30] Rabczuk T, Areias PMA, Belytschko T. A meshfree thin shell method for non-linear dynamic fracture. International Journal for Numerical Methods in Engineering 2007;72:524-48.

[31] Trahair NS, Bradford MA, Nethercot DA. The behaviour and design of steel structures to BS5950. 3rd ed. New York: Spon Press; 2001.

[32] Izzuddin BA. Nonlinear Dynamic Analysis of Framed Structures. London: Imperial College London, U.K.; 1991.

[33] Izzuddin BA, Li ZX. A co-rotational formulation for large displacement analysis of curved shells. Developments in Mechanics of Structures and Materials 2004;2:1247-53.